nature communications

Article | Article in Press

https://doi.org/10.1038/s41467-026-79635-x

Control of out-of-plane anti-damping spin torque with a canted ferromagnetic spin source

Received: 1 March 2026

Accepted: 22 October 2026

Published online: 27 November 2026

Check for updates

Xiaoxi Huang[1,11] ✉, Daniel A. Pharis[1,11], Hang Zhou[2], Zishen Tian[3,8], Thow Min Jerald Cham[1], Zhaoyang Wang[4], Yuhan Liang[1], Kyoungjun Lee[5], Yilin Evan Li[6], Maciej Olszewski[1], Di Yi[4], Chang-Beom Eom[5], Darrell G. Schlom[6,7,10], Lane W. Martin[3,8,9], Ding-Fu Shao[2] & Daniel C. Ralph[1,7] ✉

To achieve efficient anti-damping switching of nanoscale magnetic memories with perpendicular magnetic anisotropy using spin-orbit torque requires that the anti-damping spin-orbit torque have a strong out-of-plane component. The spin anomalous Hall effect and the planar Hall effect spin current produced by a ferromagnetic layer are candidate mechanisms for producing such an out-of-plane anti-damping torque, but both require that the magnetic moment of the spin source layer be canted partly out of the sample plane at zero applied magnetic field. Here we demonstrate such a canted configuration for a ferromagnetic $SrRuO_3$ layer, and we characterize all vector components of the torque that it produces, including non-zero out-of-plane anti-damping torques. We verify that the out-of-plane spin component can be tuned by the orientation of the magnetic moment, with significant contributions from both the spin anomalous Hall effect and the planar Hall effect spin current.

High-density magnetic random access memory (MRAM), which for thermal stability must be based on magnetic layers with perpendicular magnetic anisotropy (PMA), is attractive for its natural non-volatility and excellent endurance as compared to competing technologies [1,2]. Anti-damping spin-orbit torque exerted by spin currents generated within materials having strong spin-orbit interactions is a leading candidate for enhancing the write efficiency in such memories to make them competitive for energy-constrained applications [3–12]. Unfortunately, spin-source materials with high symmetry can only produce anti-damping spin-orbit torque with orientation within the sample plane, which means that they are not capable of driving efficient anti-damping switching of nanoscale PMA magnets [13,14]. Efficient switching of nanoscale PMA magnets by anti-damping spin-orbit-torque requires spin-source materials in which the symmetry constraints are relaxed either by a low-symmetry crystal structure [15–19] or magnetic order [20–26], to allow a component of out-of-plane anti-damping torque. Modeling suggests that an out-of-plane damping-like torque efficiency $\xi^{z}_{DL} \approx 0.05$ is necessary to allow a 40 nm three-terminal spin-orbit-torque MRAM device to achieve energy efficiency better than conventional spin-transfer-torque MRAM [27], while an optimized 20 nm two-terminal geometry in which out-of-plane damping-like torque from both SOT and conventional spin-transfer

[1]Department of Physics, Cornell University, Ithaca, USA. [2]Key Laboratory of Materials Physics, Institute of Solid-State Physics, HFIPS, Chinese Academy of Sciences, Hefei, China. [3]Department of Materials Science and Engineering, University of California, Berkeley, CA, USA. [4]State Key Laboratory of New Ceramics and Fine Processing, School of Materials Science and Engineering, Tsinghua University, Beijing, China. [5]Department of Materials Science and Engineering, University of Wisconsin-Madison, Wisconsin, USA. [6]Department of Materials Science and Engineering, Cornell University, Ithaca, USA. [7]Kavli Institute at Cornell for Nanoscale Science, Ithaca, NY, USA. [8]Rice Advanced Materials Institute, Rice University, Houston, TX, USA. [9]Department of Materials Science and NanoEngineering, Chemistry, and Physics and Astronomy, Rice University, Houston, TX, USA. [10]Leibniz-Institut für Kristallzüchtung, Berlin, Germany. [11]These authors contributed equally: Xiaoxi Huang, Daniel A. Pharis. xh384@cornell.edu; dcr14@cornell.edu

torque act in concert may provide a write energy comparable even to SRAM for $\xi^{Z}_{DL} > 0.052$[28]. Research on developing spin-source materials for out-of-plane anti-damping torque has so far fallen short of these thresholds, except for perhaps the low-symmetry van der Waals semimetal $TaIrTe_4$[18,29,30]. Nonetheless, generating out-of-plane anti-damping torque with low-symmetry van der Waals materials requires domain-free flakes completely free of monolayer steps, so low-symmetry van der Waals materials are unlikely to be a solution for a manufacturable technology.

Here we pursue the strategy of generating an out-of-plane anti-damping torque with a ferromagnetic spin source layer in which the orientation of the ferromagnetic moment provides the required symmetry breaking. Several mechanisms have been proposed and demonstrated with initial experiments for how ferromagnets may be used as a source of spin current with a spin orientation that is controllable by changing the magnetization direction [31,32]: e.g., via the spin anomalous Hall effect (AHE) [20,22,33,34], the planar Hall effect (PHE) spin current [20,35,36], or spin rotation or spin swapping at a magnetic interface [37–41]. Initial experiments suggest that the spin AHE and the PHE spin current are particularly promising. To generate a vertically flowing spin current with an out-of-plane spin component via either of these mechanisms requires that the magnetization of the spin-source layer be canted partially out of the sample plane (i.e., neither fully in the sample plane nor fully perpendicular to the plane): the out-of-plane anti-damping torque due to the spin AHE is predicted to be proportional to $m_Y m_Z$ and that due to the PHE spin-current mechanism is predicted to be proportional to $m_X m_Z^2$[20]. (Here $\hat{\mathbf{m}}$ is the magnetic orientation, $\hat{\mathbf{X}}$ is the direction of the in-plane applied charge current, and $\hat{\mathbf{Z}}$ is perpendicular to the sample plane.) The strength of the underlying physical mechanisms for both the spin AHE and PHE spin currents have been measured previously using samples with either in-plane magnetizations [22,33] or with magnets canted using large saturating magnetic fields [34–36], with efficiencies as large as $\xi^{Y}_{DL} = 0.25$ for the in-plane torque efficiency generated by in-plane-magnetized $L1_0$ FePt [33] via the spin AHE. The challenge with using these mechanisms to generate out-of-plane anti-damping torque for practical applications is to stabilize a partially-canted magnetic configuration with zero applied magnetic field. Thin-film samples governed entirely by shape anisotropy and first-order interfacial anisotropy have either purely in-plane or PMA configurations, so to have a stable partially-canted magnetic configuration requires use of magneto-crystalline anisotropy.

Results

The electric-field-generated spin current produced by a ferromagnetic spin-source layer can have a part with the symmetry of the conventional in-plane spin-orbit torque that does not depend on the magnetization direction (Fig. 1a) plus a part that does depend on the magnetization direction [31]. The geometries of the magnetization-dependent spin currents generated by the PHE and AHE [20] are shown in Fig. 1b, c for two different orientations of the canted magnetization relative to an applied electric field, **E**. Both the PHE and AHE give rise to spin currents with their spin polarization aligned with magnetization of the spin-source layer, but with different flow directions: for the PHE spin current the flow is parallel to $\hat{\mathbf{m}}(\hat{\mathbf{m}} \cdot \mathbf{E})$ (Fig. 1b) and for the spin AHE the flow is along $\hat{\mathbf{m}} \times \mathbf{E}$ (Fig. 1c). To achieve a vertically flowing spin current with an out-of-plane spin component, therefore, the PHE can contribute when the magnetization has a canted component in the $\hat{\mathbf{X}}$-$\hat{\mathbf{Z}}$ plane, and the AHE can similarly contribute when the magnetization has a canted component in the $\hat{\mathbf{Y}}$-$\hat{\mathbf{Z}}$ plane. As a function of the angle ψ of the applied electric field relative to the projection of the canted magnetization onto the sample plane, this means that the out-of-plane anti-damping torque should have a $\cos(\psi)$ dependence for the PHE spin current and a $\sin(\psi)$ dependence for the spin AHE. These results can be generalized: based on a symmetry analysis any time-reversal-odd spin current contributing to an out-of-plane anti-damping torque should give a $\cos(\psi)$ dependence, and any time-reversal-even spin current should give a $\sin(\psi)$ dependence (see Supplementary Information Section 12).

To achieve a magnetic spin-source layer with a partially-canted magnetization at zero applied magnetic field, we employ $SrRuO_3$ as the spin source [42–44] and deposit it on vicinal (001)-oriented $SrTiO_3$ substrates with a miscut angle around 0. 1° and a miscut direction close to [010] (Methods). $SrRuO_3$ is an itinerant ferromagnet with a bulk Curie temperature T_C ~ 160 K [45,46] and an orthorhombic crystal structure with lattice parameters $a_o = 5.5670$ Å, $b_o = 5.5304$ Å, and $c_o = 7.8446$ Å(the subscript o denotes orthorhombic structure) [47]. In the bulk, the magnetic easy axis aligns with $[010]_o$, which we will call the b axis [48], with a large magnetocrystalline anisotropy field, ~ 12 T [49]. When deposited on cubic, well-oriented (001)-$SrTiO_3$ substrates, $SrRuO_3$ thin films can grow epitaxially with six different domain configurations (see Supplementary Information Section 1). Nevertheless, by nucleating growth from step edges on a vicinal substrate, a single domain can be made dominant [50,51]. With this method we achieve the predominant epitaxial configuration shown schematically in Fig. 2a, a $(110)_o$-oriented $SrRuO_3$ film with $SrRuO_3[110]_o \| SrTiO_3[001]$, $SrRuO_3[001]_o \|$ STO [010], and $SrRuO_3[\bar{1}10]_o \|$ STO [100], resulting in the bulk magnetic easy axis (i.e., the b axis) canted uniformly away from the surface normal [48]. We verified this growth orientation using x-ray diffraction with reciprocal space mapping (Supplementary Information Section 1). Unsuccessful growths, in which more than one domain type are present, can also be detected by measurements of anomalous Hall effect versus out-of-plane magnetic field, because the different domain types can have different coercive fields (Fig. S4). For convenience in the following, we will adopt pseudo-cubic (pc) notation for $SrRuO_3$ based on the $SrTiO_3$ crystal axes, so that $[100]_{pc}$, $[010]_{pc}$ and $[001]_{pc}$ are parallel to $[\bar{1}10]_o$, $[001]_o$ and $[110]_o$.

In thin films of $SrRuO_3$ the orientation of the canted easy axis is tunable by oxygen octahedral rotation and need not lie exactly along the b axis [52–54]. We therefore performed angular-dependent magnetoresistance measurements to determine the orientation of the magnetic easy axis in our thin films [52,54]. The device geometry is shown in Fig. 2b, where a longitudinal voltage (V_{XX}) is measured while rotating an external magnetic field (**B**) in the plane perpendicular to the applied current. This magnetoresistance measurement was performed on devices oriented at in-plane angles from 0° to 90° at every 15°, to identify both the magnetic canting direction and canting angle. A representative angular-dependent magnetoresistance measurement with the magnetic field rotated in the $[001]_{pc}$-$[100]_{pc}$ plane is shown in Fig. 2c, where the jumps around 115° (295°) in resistance indicate the orientation of the magnetic hard axis (Supplementary Information Section 2). Since the easy-axis angle (θ_C) is 90° from the hard axis, for the 20 nm $SrRuO_3$ film θ_C ~ 25° away from $[001]_{pc}$ towards $[100]_{pc}$. Additional details about the determination of the canting angle are described in Supplementary Information Section 2. The canting angles of $SrRuO_3$ for thicknesses of 5, 20, and 30 nm are summarized in Fig. 2d, consistent with previous work [54,55]. We also studied 10 nm $SrRuO_3$ samples, but did not achieve predominantly single-domain films in those growths. (See Supplementary Information Section 5 and Supplementary Figs. S9 and S10).

For spin-torque studies, after the $SrRuO_3$ films were grown they were transferred through air to a separate vacuum system for deposition of a 5 nm thick $Ni_{80}Fe_{20}$ (Py) layer by magnetron sputtering on top of the $SrRuO_3$ (Methods). The Py layer has within-plane magnetic anisotropy. For thin $SrRuO_3$ samples (5 nm), where a single domain in the $SrRuO_3$ can be easily achieved (Fig. S4b), the spin-torque measurements were performed on the as-grown samples,

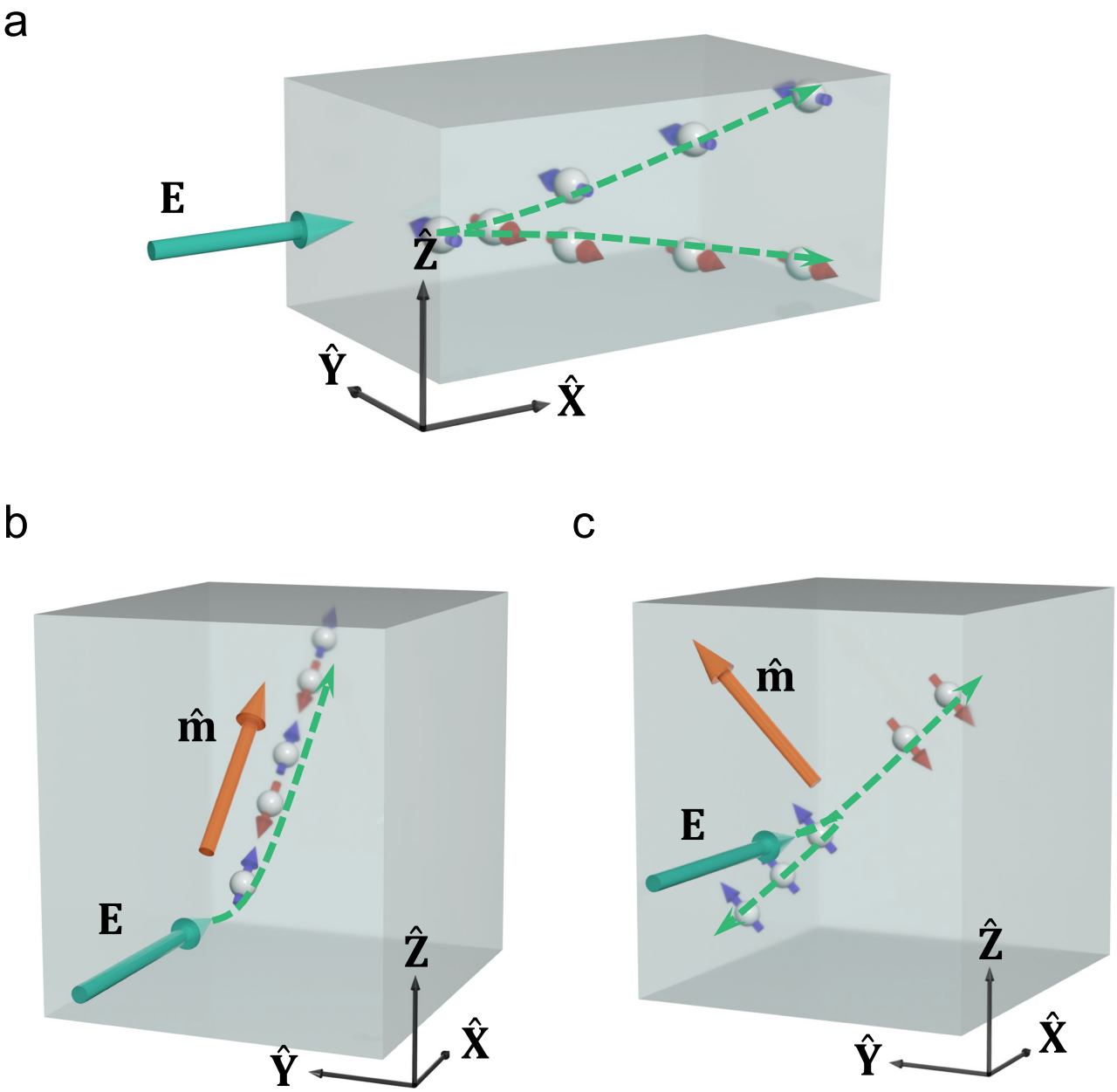


Fig. 1 | Tilted spin currents produced by a canted magnetization. a Illustration of the spin current allowed by symmetry for a non-magnetic material with high crystal symmetry, for which a spin current flowing in the $\hat{\mathbf{Z}}$ direction must have spin polarization oriented in the $\pm\hat{\mathbf{Y}}$ direction. **b** Illustration of a tilted spin current originating from the planar Hall effect in a ferromagnet, relevant for the case in which an electric field (**E**) is applied along the $\hat{\mathbf{X}}$ direction and the magnetic moment is canted away from the $\hat{\mathbf{Z}}$ direction into the $\hat{\mathbf{X}}$ direction. **c** Illustration of a tilted spin current originating from the spin anomalous Hall effect in a ferromagnet, relevant for the case in which the magnetic moment is canted away from the $\hat{\mathbf{Z}}$ direction into the $\hat{\mathbf{Y}}$ direction.

while the thicker samples (> 5 nm) in which a second type of domain becomes more significant (Fig. S4d) were field-cooled to liquid nitrogen temperature with a magnetic field oriented along the $[100]_{pc}$ axis prior to the spin torque measurements. Scans of longitudinal resistance as a function of in-plane magnetic field at 80 K along both $[100]_{pc}$ and $[010]_{pc}$ are, to a good approximation, symmetric about zero magnetic field (Fig. S6), which indicates that any exchange bias between the $SrRuO_3$ and Py is weak.

We measured the direction and strength of current-induced spin torques in the $SrRuO_3$/Py samples using angle-dependent spin torque ferromagnetic resonance (ST-FMR) [5,15,25,56] (Methods). A schematic illustration of our ST-FMR device geometry is shown in Fig. 3a. The device consists of a $SrRuO_3$/Py strip 10 μm × 40 μm in contact with ground-signal-ground electrodes made from Ti/Pt. Strips with different in-plane orientations relative to the crystal axes were fabricated to study the dependence of spin-orbit torque generation on the angle of applied electric field (or, equivalently, the angle of applied current).

https://doi.org/10.1038/s41467-026-79635-x

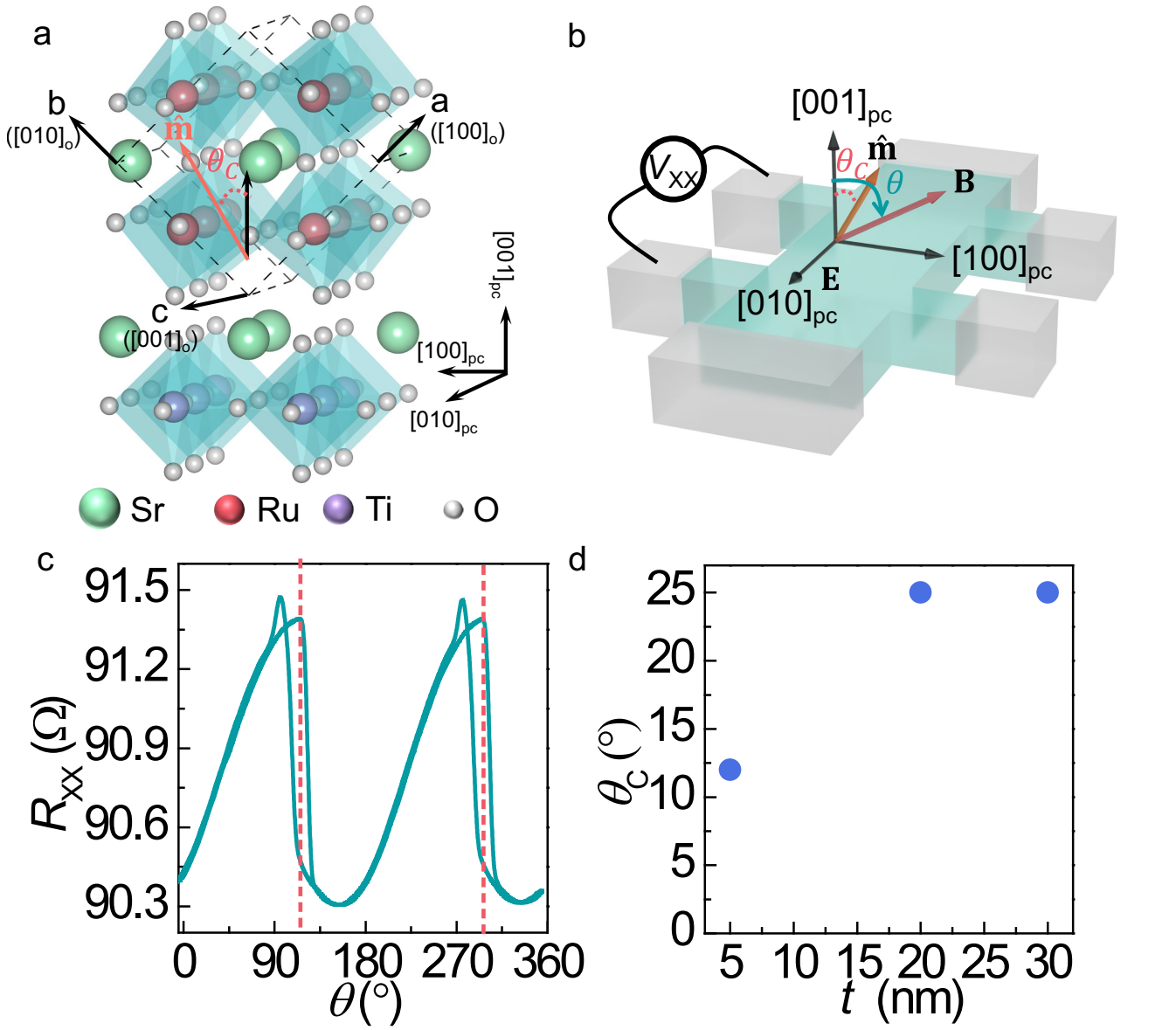


Fig. 2 | Magnetic anisotropy of $SrRuO_3$ thin films. a A side view showing the epitaxial relationship of $SrRuO_3$ grown on an (001)-oriented $SrTiO_3$ substrate, where the $[010]_{pc}$ axis points out of the page. (**a**–**c**) are the orthorhombic unit cell axes of $SrRuO_3$. In thin films, the direction of the magnetic easy axis (θ_C) can differ from the b axis. **b** Device geometry for the angular-dependent magnetoresistance measurements. A longitudinal voltage (V_{XX}) is recorded while rotating the external magnetic field (**B**) in a plane perpendicular to the applied current. θ is the external magnetic field angle from the surface normal ($[001]_{pc}$). **c** An example angular dependent magnetoresistance measurement at 10 K, where longitudinal resistance (R_{XX}) is plotted as a function of magnetic field angle θ for a sample $SrRuO_3$(20 nm)/Py (5 nm). A d.c. current of 100 μA is applied along the $[010]_{pc}$ direction and a magnetic field 6 T is rotated in the $(010)_{pc}$ plane. **d** Summary of the easy-axis tilt angle (θ_C) for $SrRuO_3$ films of various thicknesses (t) at 10 K.

On each device with a distinct orientation, we apply a microwave signal with fixed frequency and sweep the external magnetic field **B** at an angle φ to the applied electric-field direction (Fig. 3a), repeating the measurement on the same device for φ from 0° to 170°. An example ST-FMR spectrum at $\varphi = 45°$ is shown in Fig. 3b, where the mixing voltage (V_{mix}) is fit to the sum of symmetric Lorentzian, $V_S = S(\frac{\Delta^2}{(B-B_0)^2+\Delta^2})$, and anti-symmetric Lorentzian, $V_A = A(\frac{\Delta(B-B_0)}{(B-B_0)^2+\Delta^2})$. Here, S and A are the amplitudes of the symmetric and anti-symmetric components of the mixing voltage, Δ is the linewidth of the resonance peak, and B_0 is the resonant magnetic field. A pronounced difference in the amplitudes of the anti-symmetric component of the mixing voltage at positive and negative fields is observed, indicating the existence of an unconventional torque in the out-of-plane direction. To unambiguously identify the directions of the torques, symmetry analysis is necessary, since the signals generated by different components of torque have different dependencies on the orientations of the external magnetic field. If we define the current flow direction as $\hat{\mathbf{X}}$, the out-of-plane direction as $\hat{\mathbf{Z}}$, and use polar coordinates to describe the magnetic field with the azimuthal angle φ measured from the $\hat{\mathbf{X}}$ direction, then the φ dependence of the mixing voltages from X, Y, Z components of the torques are [15,25]:

$$V_A = A_{FL}^X \sin 2\varphi \sin\varphi + A_{FL}^Y \sin 2\varphi \cos\varphi + A_{DL}^Z \sin 2\varphi \quad (1)$$

https://doi.org/10.1038/s41467-026-79635-x

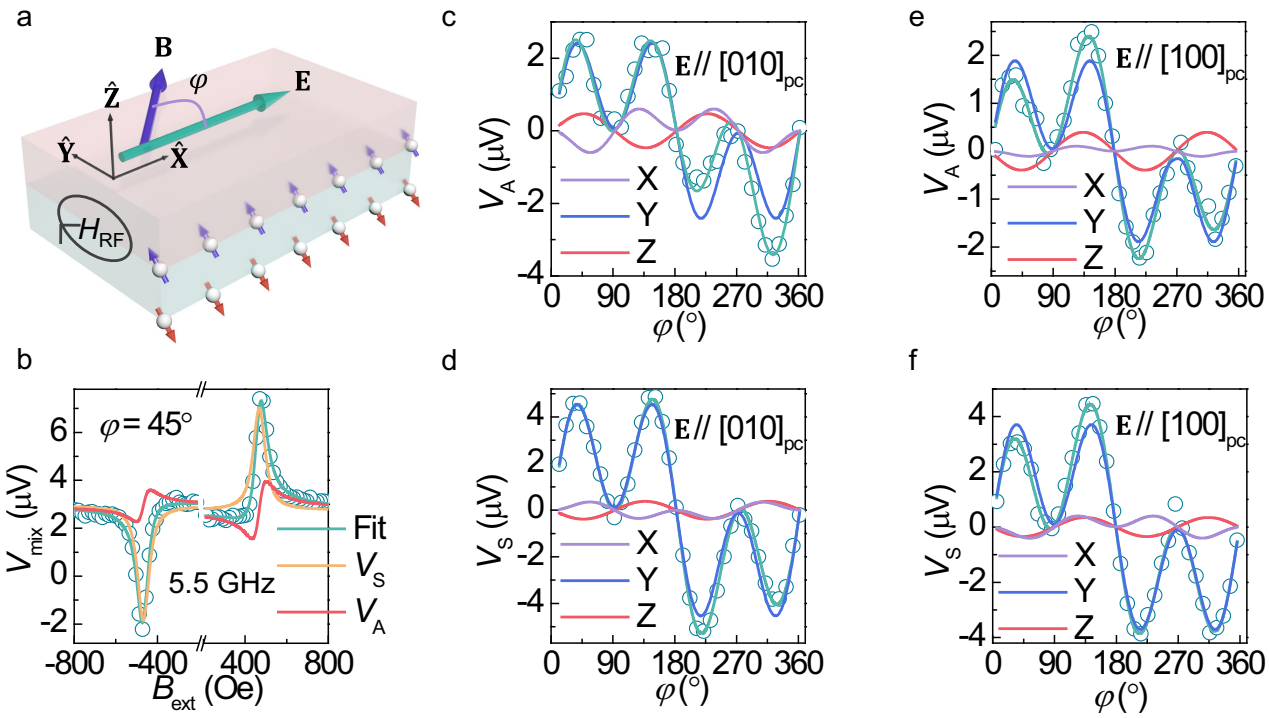


Fig. 3 | Spin torques characterized by spin-torque ferromagnetic resonance. **a** A schematic of a $SrRuO_3$ (5 nm)/Py (5 nm) bilayer used in the ST-FMR measurements. Red layer: Py; Teal layer: $SrRuO_3$; H_{RF}: Oersted field produced by the applied microwave current; **B**: external magnetic field; **E**: electric field; φ: angle between external magnetic field and microwave current. **b** Example ST-FMR spectrum, with the d.c. mixing voltage (V_{mix}) plotted as a function of external magnetic field (**B**). In this example, the ST-FMR measurement is done at 110 K with **E** approximately along $[010]_{pc}$ and φ = 45°. The curve in teal represents a fit to the mixing voltage, and the red and orange curves represent the anti-symmetric (V_A) and symmetric (V_S) components of the mixing voltage respectively. **c** Anti-symmetric mixing voltage as a function of magnetic field angle. X (purple), Y (blue), Z (red) components of the anti-symmetric mixing voltages are determined as the fit components proportional to $\sin(2\varphi)\sin\varphi$, $\sin(2\varphi)\cos\varphi$ and $\sin(2\varphi)$ respectively. **d** Symmetric mixing voltage as a function of magnetic field angle. X (purple), Y (blue) and Z (red) components of the symmetric mixing voltages are determined as the fit components proportional to $\sin(2\varphi)\cos\varphi$, $\sin(2\varphi)\cos\varphi$ and $\sin(2\varphi)$ respectively. The electric field is applied approximately along the $[010]_{pc}$ crystallographic axis in the plane for (**c**, **d**). **e**, **f** Anti-symmetric and symmetric mixing voltages as a function of magnetic field angle for an electric field applied approximately along the $[100]_{pc}$ crystallographic axis.

$$V_S = S_{DL}^X \sin 2\varphi \sin\varphi + S_{DL}^Y \sin 2\varphi \cos\varphi + S_{FL}^Z \sin 2\varphi \quad (2)$$

where S_{DL}^X, S_{DL}^Y, A_{DL}^Z are the amplitudes of the mixing voltages contributed by the X, Y, Z components of the damping-like torque; and A_{FL}^X, A_{FL}^Y, S_{FL}^Z are the amplitudes of the mixing voltages from the contributions of the X, Y, Z components of the field-like torque. Two representative angle-dependent ST-FMR results at 110 K are shown in Fig. 3c, d and Fig. 3e, f for a $SrRuO_3$ (5 nm)/Py (5 nm) sample with applied electric fields approximately parallel to $[010]_{pc}$ and $[100]_{pc}$. For both orientations of **E**, fits to both the anti-symmetric and symmetric mixing voltages require additional Z ($\sin 2\varphi$) and X ($\sin 2\varphi \sin\varphi$) components of the torques, in addition to the conventional Y component ($\sin 2\varphi \cos\varphi$). Comparing the ST-FMR results for two perpendicular electric-field directions, the anti-symmetric mixing signals corresponding to the Z component of torque have opposite signs (compare the red lines in Fig. 3c and Fig. 3e). Below we will ascribe this difference to separate contributions from the spin AHE and the PHE spin current.

We have confirmed the presence of the unconventional torque components using a second measurement technique, second harmonic Hall measurements. Angle-dependent second harmonic Hall voltage data for 100 K are shown in Fig. S12a, b for the same $SrRuO_3$ (5 nm)/Py (5 nm) sample with applied electric fields approximately parallel to $[010]_{pc}$ and $[100]_{pc}$. The Z component of the damping-like torques for electric-field along $[010]_{pc}$ and $[100]_{pc}$ have opposite signs, in agreement with the ST-FMR results.

Based on the ST-FMR measurements, the damping-like torque efficiencies can be be calculated as [57]

$$\xi_{DL}^Y = S_{DL}^Y \frac{eM_S t_{FM}}{\hbar J_e} \frac{4\Delta}{I_{rf} R_{AMR}} \frac{2B_0 + \mu_0 M_{eff}}{\sqrt{B_0(B_0 + \mu_0 M_{eff})}} \quad (3)$$

$$\xi_{DL}^Z = A_{DL}^Z \frac{eM_S t_{FM}}{\hbar J_e} \frac{4\Delta}{I_{rf} R_{AMR}} \frac{2B_0 + \mu_0 M_{eff}}{B_0 + \mu_0 M_{eff}} \quad (4)$$

where M_S (A/m) is the saturation magnetization for 5 nm of Py, t_{FM} is the thickness of the Py layer, I_{rf} is the amplitude of the microwave current within the full bilayer, J_e is the current density within the $SrRuO_3$, and $\mu_0 M_{eff}$ (T) is the effective field from the magnetic anisotropy. We calibrate I_{rf} by comparing the heating-induced change in resistance due to a microwave current to the heating-induced change of a d.c. current, and then J_e is determined from a parallel circuit model using the measured resistivities of the Py and the $SrRuO_3$ (see Supplementary Information Section 4). For the data shown in Fig. 3, I_{rf} = 2.03 mA and $J_e = 9.50 \times 10^9$ A/m^2. For the case of **E** along $[010]_{pc}$, the Y and Z components of the damping-like torque efficiencies estimated with Eq. (3) and Eq. (4) are $\xi_{DL}^Y = 0.32 \pm 0.05$ and $\xi_{DL}^Z = 0.0065 \pm 0.0009$. Given that the resistivity (ρ) of $SrRuO_3$ at 110 K is around 231 $\mu\Omega$cm, the spin Hall conductivities estimated using $\sigma_{DL} = (\hbar/2e)\xi_{DL}/\rho$ for the Y and Z components are

https://doi.org/10.1038/s41467-026-79635-x

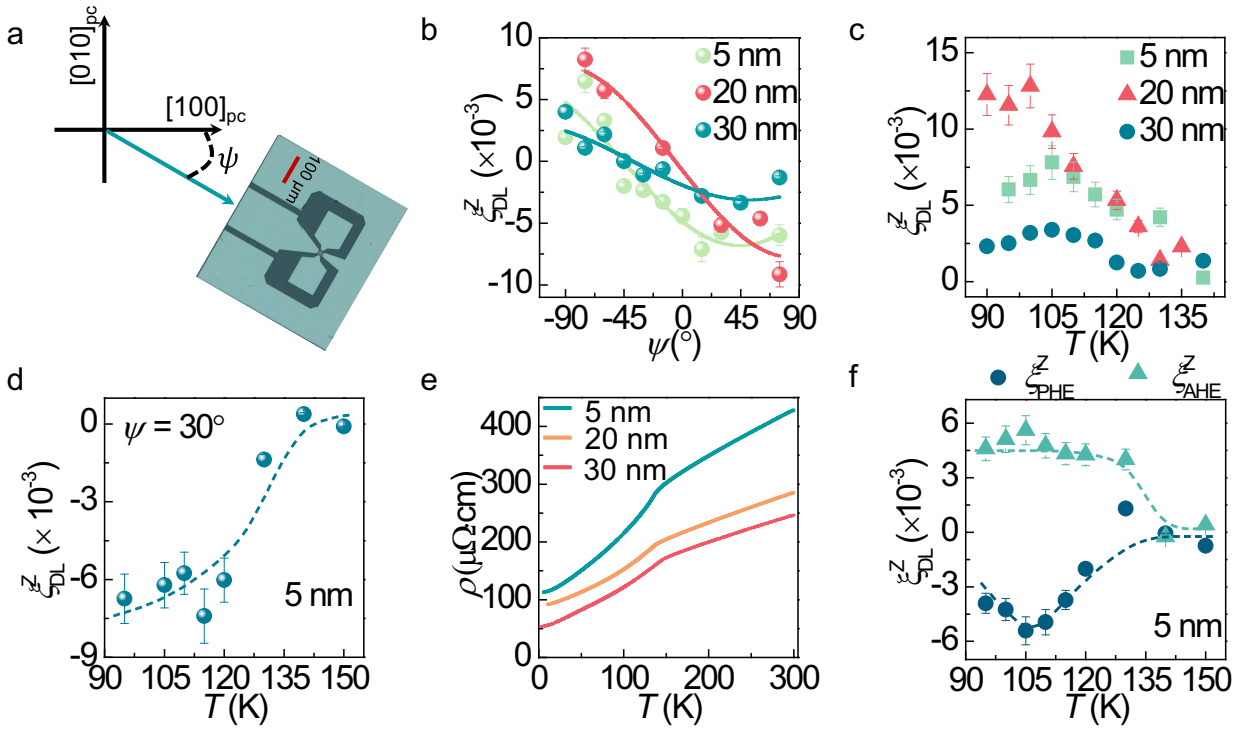


Fig. 4 | Dependence of out-of-plane anti-damping torque on the orientation of the applied electric field and temperature. a A schematic of the ST-FMR measurement geometry, for **E** is oriented at a ψ angle to $[100]_{pc}$. **b** Out-of-plane anti-damping torque efficiency as a function of ψ for a $SrRuO_3$ (5 nm)/Py (5 nm) sample (110 K, green), a $SrRuO_3$ (20 nm)/Py (5 nm) sample (110 K, red), and a $SrRuO_3$ (30 nm)/Py (5 nm) sample (105 K, teal). The solid curves represent fits to the data as a linear superposition of $\sin\psi$ and $\cos\psi$, used to determine the AHE and PHE contributions as in (**f**) below. **c** Temperature dependence of the peak out-of-plane damping-like torque efficiency for $SrRuO_3$ of 5 nm (green squares), 20 nm (red triangles) and 30 nm (teal circles) thickness. **d** Representative temperature dependent out-of-plane anti-damping torque efficiency at $\psi = 30^{\circ}$ for the $SrRuO_3$ (5 nm)/Py (5 nm) sample. The dashed line is a guide to the eye. **e** Resistivity as a function of temperature for $SrRuO_3$ of various thicknesses. The curves in teal, orange, and red represent 5 nm, 20 nm, and 30 nm thick $SrRuO_3$ samples. **f** The PHE (ξ^Z_{PHE}) and AHE (ξ^Z_{AHE}) components (circles and triangles respectively) of the out-of-plane anti-damping torque efficiencies as a function of temperature for 5 nm $SrRuO_3$. The dashed lines are guides to the eye. Error bars in (**b**–**d**) are dominated by the uncertainties of film thicknesses, and error bars in f represent fitting uncertainties.

$\sigma^Y_{DL} = (1.39 \pm 0.22) \times 10^5 (\hbar/2e)(\Omega^{-1}m^{-1})$ and $\sigma^Z_{DL} = (2.81 \pm 0.39) \times 10^3 (\hbar/2e)(\Omega^{-1}m^{-1})$. For **E** along $[100]_{pc}$, the damping-like torque efficiencies for Y and Z components are estimated to be $\xi^Y_{DL} = 0.34 \pm 0.05$ and $\xi^Z_{DL} = -0.0071 \pm 0.0010$; and the corresponding spin Hall conductivities for Y and Z component are $\sigma^Y_{DL} = (1.47 \pm 0.22) \times 10^5 (\hbar/2e)(\Omega^{-1}m^{-1})$ and $\sigma^Z_{DL} = (-3.07 \pm 0.43) \times 10^3 (\hbar/2e)(\Omega^{-1}m^{-1})$.

To investigate the origins of out-of-plane anti-damping torque, the magnetic field angle-dependent ST-FMR measurements were repeated on devices with intermediate ψ angles for the orientation of the applied electric field relative to the $[100]_{pc}$ crystal direction (Fig. 4a). The out-of-plane anti-damping torque efficiency ξ^Z_{DL} has the angular dependence shown in Fig. 4b. This behavior of ξ^Z_{DL} is in excellent agreement with the predicted dependence for the sum of torques due to the spin AHE ($\propto \sin(\psi)$) and the PHE spin current ($\propto \cos(\psi)$): $\xi^Z_{DL} = \xi^Z_{PHE}\cos\psi + \xi^Z_{AHE}\sin\psi$ for fitting parameters ξ^Z_{PHE} = -0.0048 and ξ^Z_{AHE} = 0.0049 for the 5 nm thick $SrRuO_3$.

In addition to data for the 5 nm device, Fig. 4b also shows the measured out-of-plane anti-damping torque efficiencies ξ^Z_{DL} per unit charge density as a function of the electric-field angle ψ for 20 and 30 nm $SrRuO_3$ layer thicknesses. The temperature dependences for the peak out-of-plane anti-damping torque efficiencies for $SrRuO_3$ of 5 nm, 20 nm and 30 nm are shown in Fig. 4c. We find that ξ^Z_{DL} reaches a peak value at approximately 20 nm, with $\xi^Z_{DL} = 0.013 \pm 0.001$ at 100 K. This corresponds to a peak value for the Z component of the spin Hall conductivity $\sigma^Z_{DL} = 8.5 \times 10^3 \frac{\hbar}{2e}(\Omega m)^{-1}$, qualitatively consistent (i.e., within approximately a factor of 2) of the density functional prediction (Supplementary Information Section 12). The peak torque efficiency is greater for 20 nm thick $SrRuO_3$ than for 30 nm despite the fact that the 30 nm thick layer has a comparable canting angle for the magnetization (see Fig. 2d). This difference in torque efficiency could be an indication, e.g., of competing contributions from the larger magnetization canting angle versus a less-perfect domain structure for the 30 nm films (Fig. S4), or a contribution from an interfacial torque mechanism and not just a bulk mechanism.

The temperature dependence of ξ^Z_{DL} for a $SrRuO_3$ (5 nm)/Py (5 nm) is shown in Fig. 4d for the electric-field angle $\psi = 30^{\circ}$, near which the magnitude of ξ^Z_{DL} is maximized. The magnitude of ξ^Z_{DL} decreases with increasing temperature and approaches zero near 135 K, just below the bulk Curie temperature (and remains zero up to room temperature, see Fig. S11). (The Curie temperature (T_C) of the $SrRuO_3$ thin films of various thicknesses can be identified from the kink in the resistivity versus temperature curves (Fig. 4e), yielding values of T_C between 130 K and 140 K). Based on measurements at $\psi = 0^{\circ}$ and 90°, we can also separate the temperature dependence due to the PHE ($\propto \cos(\psi)$) and spin AHE ($\propto \sin(\psi)$) spin current mechanisms (Fig. 4f). The spin AHE contribution has very little temperature dependence between liquid-nitrogen temperature and 130 K, while the PHE spin current contribution varies strongly in the same temperature range. We speculate that the time-even spin AHE contribution is due primarily to intrinsic spin-orbit coupling within the $SrRuO_3$ band structure and is therefore relatively temperature-independent well below

the Curie temperature, while the PHE spin current is odd under time reversal and is therefore more likely to depend on extrinsic scattering and other processes which can vary with temperature.

The maximum value of the out-of-plane anti-damping torque that we measure, $\xi^{Z}_{DL} = 0.013 \pm 0.001$, remains below the threshold predicted by modeling to be necessary to directly drive anti-damping switching in nanoscale PMA devices more efficiently than conventional spin-transfer torque (~ 0.05 [27,28]). For this reason, we have not attempted to investigate switching in nanoscale structures. However, as an additional confirmation of the existence of out-of-plane anti-damping torque we have demonstrated field-free deterministic switching of a PMA magnetic layer in larger, 10 μm-scale, structures where magnetic reversal happens via domain-wall motion. In this regime, the critical current for switching is determined primarily by the conventional in-plane component of spin-orbit torque, and even a weak out-of-plane anti-damping torque can provide the symmetry-breaking needed to make the switching deterministic at zero applied magnetic field. We performed current-induced magnetization switching experiments on PMA Ti/$Co_{20}Fe_{60}B_{20}$/MgO structues with either Pt (5 nm) or $SrRuO_3$ (10 nm) serving as the spin source material underneath the Ti layer (Supplementary Information Section 8 and Fig. S15). Since Pt produces only conventional anti-damping torque within the sample plane, it requires a symmetry-breaking external magnetic field along the current direction to achieve deterministic switching of the PMA magnet (Supplementary Information Fig. S13). In contrast, the spin current produced by $SrRuO_3$ allows deterministic switching at zero field, with the sign of switching insensitive to at least a 30 Oe field applied either parallel or antiparallel to the current direction Fig. S15b–d).

In summary, we have demonstrated a strategy for achieving a partly-canted magnetization configuration in a magnetic spin-source layer at zero applied magnetic field, and have shown that this configuration allows for the generation of vertically-flowing spin current with an out-of-plane spin component, which can therefore exert an out-of-plane anti-damping spin-orbit torque on an adjacent magnetic layer. The use of the ferromagnetic moment to provide the symmetry-breaking needed to enable an out-of-plane anti-damping torque circumvents the challenges posed by low-crystalline-symmetry materials and antiferromagnets for switching magnetic memories with perpendicular magnetic anisotropy. Based on the dependence of the out-of-plane torques on the angle of the applied electric field relative to the canted magnetization, the out-of-plane anti-damping torques generated by $SrRuO_3$ can be well-described as due to the sum of a spin AHE and a PHE spin current. The maximum out-of-plane torque efficiency that we measure, $\xi^{Z}_{DL} = 0.013 \pm 0.001$ is still below the threshold needed for spin-orbit-torque MRAM to achieve better energy efficiency than conventional spin-transfer-torque MRAM. (Table S1 presents a list of materials systems in which out-of-plane anti-damping torques have been measured quantitatively.) Nonetheless, our study opens the door to explore torque generation by other magnetic materials in which magnetocrystalline anisotropy might be used to stabilize similar partly-canted magnetization configurations [58].

Methods

Sample preparation

$SrRuO_3$ thin films were grown with pulsed laser deposition (PLD). The thin films were grown on slightly miscut (001)-oriented $SrTiO_3$ substrates at 700 °C, 100 mTorr oxygen partial pressure, and a laser energy of 1.5 J/cm^2 at 2 Hz. After growth, the samples were cooled down at 5 °C/min to room temperature at an atmospheric oxygen pressure. The detection magnet layer (Py) was deposited in an AJA magnetron sputterer system with a base pressure of 2×10^{-8} Torr. A 1.5 nm Ta capping layer was then deposited on the Py to inhibit oxidation.

Device fabrication

ST-FMR and Hall devices with various ψ angles to the crystal axis were patterned using a Heidelberg laser direct writer. The $SrRuO_3$ layer was etched with $NaIO_4$ solution (0.1 mol/L), and other layers were etched by ion milling. Contacts made from Pt (100 nm)/Ti (5 nm) were sputtered in an AJA chamber and then lifted off. For ST-FMR devices, strips with dimension 10 μm × 40 μm were in contact with ground-signal-ground electrodes. For Hall devices, the dimensions of the Hall bar were 20 μm × 50 μm.

Magnetoresistance measurement

Hall devices with various in-plane orientations (ψ) were patterned on $SrRuO_3$/Py samples. A direct current of 100 μA was applied with Keithley 2400 d.c. current source meter in the current channel and a longitudinal voltage was measured with Keithley 2181A nanovoltmeter. For the magnetic-field-angle dependent magnetoresistance measurements, an external magnetic field of several Tesla was rotated in a plane perpendicular to the applied current. The measurements were repeated on devices with in-plane orientation ψ from 0° to 90° at every 15° to identify both the magnet canting direction and canting angle. To investigate the exchange coupling between $SrRuO_3$ and Py, the external magnetic field was swept in the plane from positive to negative along the current direction, while recording the longitudinal voltage. The measurement was repeated on devices oriented along both the $[100]_{pc}$ and $[010]_{pc}$ directions.

ST-FMR measurement

ST-FMR devices with ground-signal-ground (GSG) contacts were fabricated from the $SrRuO_3$/Py bilayers. A microwave current at a fixed frequency (5 GHz–5.5 GHz) and power was applied. A dc mixing voltage was measured with a DSP lock-in amplifier while sweeping the external magnetic field from positive to negative at a fixed angle (φ) to the applied current. The same ST-FMR measurement was repeated at magnetic field angles φ from 0° to 170° at every 10°. This magnetic-field-angle-dependent ST-FMR measurement was performed on devices with applied-current angles ψ (in the film plane relative to the $[100]_{pc}$ direction) from 0° to 165° in 15° increments. The temperature-dependent ST-FMR measurements were carried out in a home-built cryostat cooled by liquid nitrogen.

Data availability

The data generated in this study are publicly available in the Zenodo repository at https://doi.org/10.5281/zenodo.20504746.

References

1. Bhatti, S. et al. Spintronics based random access memory: a review. *Mater. Today* **20**, 530–548 (2017).
2. Dieny, B. & Chshiev, M. Perpendicular magnetic anisotropy at transition metal/oxide interfaces and applications. *Rev. Mod. Phys.* **89**, 025008 (2017).
3. Mihai Miron, I. et al. Current-driven spin torque induced by the Rashba effect in a ferromagnetic metal layer. *Nat. Mater.* **9**, 230–234 (2010).
4. Miron, I. M. et al. Perpendicular switching of a single ferromagnetic layer induced by in-plane current injection. *Nature* **476**, 189–193 (2011).
5. Liu, L., Moriyama, T., Ralph, D. & Buhrman, R. Spin-torque ferromagnetic resonance induced by the spin Hall effect. *Phys. Rev. Lett.* **106**, 036601 (2011).
6. Liu, L. et al. Spin-torque switching with the giant spin Hall effect of tantalum. *Science* **336**, 555–558 (2012).
7. Mellnik, A. R. et al. Spin-transfer torque generated by a topological insulator. *Nature* **511**, 449–451 (2014).

8. Fan, Y. et al. Magnetization switching through giant spin-orbit torque in a magnetically doped topological insulator heterostructure. *Nat. Mater.* **13**, 699–704 (2014).
9. Han, J. et al. Room-temperature spin-orbit torque switching induced by a topological insulator. *Phys. Rev. Lett.* **119**, 077702 (2017).
10. Wang, Y. et al. Room temperature magnetization switching in topological insulator-ferromagnet heterostructures by spin-orbit torques. *Nat. Commun.* **8**, 1364 (2017).
11. Nan, T. et al. Anisotropic spin-orbit torque generation in epitaxial $SrIrO_3$ by symmetry design. *PNAS* **116**, 16186–16191 (2019).
12. Huang, X. et al. Novel spin-orbit torque generation at room temperature in an all-oxide epitaxial $La_{0.7}Sr_{0.3}MnO_3$/sriro$_3$ system. *Adv. Mater.* **33**, 2008269 (2021).
13. Garello, K. et al. Symmetry and magnitude of spin–orbit torques in ferromagnetic heterostructures. *Nat. Nanotechnol.* **8**, 587–593 (2013).
14. Zhang, C., Fukami, S., Sato, H., Matsukura, F. & Ohno, H. Spin-orbit torque induced magnetization switching in nano-scale ta/cofeb/mgo. *Appl. Phys. Lett.* **107**, 012401 (2015).
15. MacNeill, D. et al. Control of spin-orbit torques through crystal symmetry in WTe_2/ferromagnet bilayers. *Nat. Phys.* **13**, 300–305 (2017).
16. Liu, L. et al. Symmetry-dependent field-free switching of perpendicular magnetization. *Nat. Nanotechnol.* **16**, 277–282 (2021).
17. DC, M. et al. Observation of anti-damping spin-orbit torques generated by in-plane and out-of-plane spin polarizations in $MnPd_3$. *Nat. Mater.* **22**, 591–598 (2023).
18. Liu, Y. et al. Field-free switching of perpendicular magnetization at room temperature using out-of-plane spins from tairte$_4$. *Nat. Electron.* **6**, 732–738 (2023).
19. Patton, M. et al. Symmetry control of unconventional spin-orbit torques in IrO_2. *Adv. Mater.* **35**, 2301608 (2023).
20. Taniguchi, T., Grollier, J. & Stiles, M. D. Spin-transfer torques generated by the anomalous Hall effect and anisotropic magnetoresistance. *Phys. Rev. Appl.* **3**, 044001 (2015).
21. Železny`, J., Zhang, Y., Felser, C. & Yan, B. Spin-polarized current in noncollinear antiferromagnets. *Phys. Rev. Lett.* **119**, 187204 (2017).
22. Iihama, S. et al. Spin-transfer torque induced by the spin anomalous Hall effect. *Nat. Electron.* **1**, 120–123 (2018).
23. Nan, T. et al. Controlling spin current polarization through non-collinear antiferromagnetism. *Nat. Commun.* **11**, 4671 (2020).
24. Chen, X. et al. Observation of the antiferromagnetic spin Hall effect. *Nat. Mater.* **20**, 800–804 (2021).
25. Bose, A. et al. Tilted spin current generated by the collinear antiferromagnet ruthenium dioxide. *Nat. Electron.* **5**, 267–274 (2022).
26. Chen, H. et al. Pure spin current polarizer enabled by antiferromagnetic insulator. *Nat. Commun.* **16**, 6257 (2025).
27. Liao, Y.-C. et al. Spin-orbit-torque material exploration for maximum array-level read/write performance. In *2020 IEEE International Electron Devices Meeting (IEDM)*, 13–6 (IEEE, 2020).
28. Shazon, M. N. H., Kumar, P., Liu, L., Ralph, D. C. & Naeemi, A. Modeling and optimization of two-terminal spin-orbit-torque MRAM. *IEEE Transactions on Electron Devices***in press** (2026).
29. Zhang, Y. et al. Room temperature field-free switching of perpendicular magnetization through spin-orbit torque originating from low-symmetry type II Weyl semimetal. *Sci. Adv.* **9**, eadg9819 (2023).
30. Bainsla, L. et al. Large out-of-plane spin-orbit torque in topological Weyl semimetal TaIrTe$_4$. *Nat. Commun.* **15**, 4649 (2024).
31. Amin, V. P., Li, J., Stiles, M. D. & Haney, P. M. Intrinsic spin currents in ferromagnets. *Phys. Rev. B* **99**, 220405 (2019).
32. Davidson, A., Amin, V. P., Aljuaid, W. S., Haney, P. M. & Fan, X. Perspectives of electrically generated spin currents in ferromagnetic materials. *Phys. Lett. A* **384**, 126228 (2020).
33. Seki, T., Iihama, S., Taniguchi, T. & Takanashi, K. Large spin anomalous Hall effect in $L1_0$-fept: Symmetry and magnetization switching. *Phys. Rev. B* **100**, 144427 (2019).
34. Montoya, E. A., Pei, X. & Krivorotov, I. N. Anomalous Hall spin current drives self-generated spin–orbit torque in a ferromagnet. *Nat. Nanotechnol.* **20**, 353–359 (2025).
35. Safranski, C., Montoya, E. A. & Krivorotov, I. N. Spin-orbit torque driven by a planar Hall current. *Nat. Nanotechnol.* **14**, 27–30 (2019).
36. Safranski, C., Sun, J. Z., Xu, J.-W. & Kent, A. D. Planar Hall-driven torque in a ferromagnet/nonmagnet/ferromagnet system. *Phys. Rev. Lett.* **124**, 197204 (2020).
37. Saidaoui, H. B. M. & Manchon, A. Spin-swapping transport and torques in ultrathin magnetic bilayers. *Phys. Rev. Lett.* **117**, 036601 (2016).
38. Humphries, A. M. et al. Observation of spin-orbit effects with spin rotation symmetry. *Nat. Commun.* **8**, 911 (2017).
39. Baek, S.-h C. et al. Spin currents and spin-orbit torques in ferromagnetic trilayers. *Nat. Mater.* **17**, 509–513 (2018).
40. Amin, V. P., Zemen, J. & Stiles, M. D. Interface-generated spin currents. *Phys. Rev. Lett.* **121**, 136805 (2018).
41. Yang, Q. et al. Field-free spin-orbit torque switching in ferromagnetic trilayers at sub-ns timescales. *Nat. Commun.* **15**, 1814 (2024).
42. Ou, Y. et al. Exceptionally high, strongly temperature dependent, spin Hall conductivity of $SrRuO_3$. *Nano Lett.* **19**, 3663–3670 (2019).
43. Wei, J. et al. Enhancement of spin-orbit torque by strain engineering in srruo$_3$ films. *Adv. Funct. Mater.* **31**, 2100380 (2021).
44. Zhou, J. et al. Modulation of spin-orbit torque from $SrRuO_3$ by epitaxial-strain-induced octahedral rotation. *Adv. Mater.* **33**, 2007114 (2021).
45. Longo, J., Raccah, P. & Goodenough, J. Magnetic properties of $SrRuO_3$ and $CaRuO_3$. *J. Appl. Phys.* **39**, 1327–1328 (1968).
46. Schreiber, N. J. et al. Enhanced t_c in $SrRuO_3$/$DyScO_3$ (110) thin films with high residual resistivity ratio. *APL Mater.* **11**, 111101 (2023).
47. Jones, C., Battle, P., Lightfoot, P. & Harrison, W. The structure of srruo$_3$ by time-of-flight neutron powder diffraction. *Acta Crystallogr. Sect. C: Cryst. Struct. Commun.* **45**, 365–367 (1989).
48. Gan, Q., Rao, R., Eom, C., Wu, L. & Tsui, F. Lattice distortion and uniaxial magnetic anisotropy in single domain epitaxial (110) films of $SrRuO_3$. *J. Appl. Phys.* **85**, 5297–5299 (1999).
49. Koster, G. et al. Structure, physical properties, and applications of $SrRuO_3$ thin films. *Rev. Mod. Phys.* **84**, 253 (2012).
50. Gan, Q., Rao, R. & Eom, C. Control of the growth and domain structure of epitaxial $SrRuO_3$ thin films by vicinal (001) $SrTiO_3$ substrates. *Appl. Phys. Lett.* **70**, 1962–1964 (1997).
51. Jiang, J., Tian, W., Pan, X., Gan, Q. & Eom, C. Domain structure of epitaxial $SrRuO_3$ thin films on miscut (001) $SrTiO_3$ substrates. *Appl. Phys. Lett.* **72**, 2963–2965 (1998).
52. Lu, W., Yang, P., Song, W. D., Chow, G. M. & Chen, J. S. Control of oxygen octahedral rotations and physical properties in $SrRuO_3$ films. *Phys. Rev. B* **88**, 214115 (2013).
53. Lu, W. et al. Strain engineering of octahedral rotations and physical properties of $SrRuO_3$ films. *Sci. Rep.* **5**, 10245 (2015).
54. Liu, L. et al. Current-induced magnetization switching in all-oxide heterostructures. *Nat. Nanotechnol.* **14**, 939–944 (2019).
55. Yoo, Y. et al. Diverse effects of two-dimensional and step flow growth mode induced microstructures on the magnetic anisotropies of $SrRuO_3$ thin films. *Appl. Phys. Lett.***89** (2006).
56. Fang, D. et al. Spin-orbit-driven ferromagnetic resonance. *Nat. Nanotechnol.* **6**, 413–417 (2011).
57. Karimeddiny, S., Mittelstaedt, J. A., Buhrman, R. A. & Ralph, D. C. Transverse and longitudinal spin-torque ferromagnetic resonance for improved measurement of spin-orbit torque. *Phys. Rev. Appl.* **14**, 024024 (2020).
58. Belashchenko, K. Exchange-driven spin hall effect in anisotropic ferromagnets. *Phys. Rev. B* **109**, 054409 (2024).

Author contributions

X.H. and D.C.R. conceived and designed the research. Z.T., Y.E.L., K.L., and Z.W. carried out the oxide thin film growth. X.H. and M.O. performed the magnetron sputtering. X.H. and T.M.J.C. carried out the low temperature ST-FMR measurements with help from D.A.P.; X.H. did the device fabrication with help from D.A.P.; X.H. and D.A.P. performed the angle-dependent magnetoresistance measurements. X.H. conducted the current-induced magnetization switching experiments with help from Y.L.; T.M.J.C. simulated the angular-dependent magnetoresistance. H.Z. and D.F.S. performed the phenomenological symmetry analysis and first-principles calculations. D.Y., C.B.E., D.G.S., and L.W.M. gave suggestions on the experiments. All authors discussed the results and assisted in the preparation of the manuscript.

Funding

X.H. was supported by the US Department of Energy (DOE), Office of Basic Energy Sciences (BES) under award number DE-SC0017671. D.P., D.G.S., and D.C.R. acknowledge support from SUPREME, one of seven centers in JUMP 2.0, a Semiconductor Research Corporation program sponsored by DARPA. Z.T. acknowledges that this work is supported by the Air Force Office of Scientific Research under award number FA9550-24-1-0266. Any opinions, findings, and conclusions or recommendations expressed in this material are those of the author(s) and do not necessarily reflect the views of the United States Air Force. L.W.M. acknowledges support from the National Science Foundation (NSF) under Grant DMR-2329111. T.M.J.C. and M.O. were supported in part by the NSF under DMR-2104268. C.B.E. acknowledges support from the Vannevar Bush Faculty Fellowship (ONR N00014-20-1-2844), the Gordon and Betty Moore Foundation's EPiQS Initiative, Grant No. GBMF9065, and the NSF through the Designing Materials to Revolutionize and Engineer our Future (DMREF) program (DMREF-2522669). Thin film synthesis at the University of Wisconsin-Madison was supported by the U.S. Department of Energy, Office of Science, Office of Basic Energy Sciences, under Award No. DE-FG02-06ER46327. The devices were fabricated using the shared facilities of the Cornell NanoScale Facility, a member of the National Nanotechnology Coordinated Infrastructure (supported by the NSF via grant NNCI-2025233) and the facilities of the Cornell Center for Materials Research.

Competing interests

The authors declare no competing interests.

Additional information

Supplementary information The online version contains supplementary material available at https://doi.org/10.1038/s41467-026-79635-x.

Correspondence and requests for materials should be addressed to Xiaoxi Huang or Daniel C. Ralph.

Peer review information *Nature Communications* thanks the anonymous, reviewers for their contribution to the peer review of this work. A peer review file is available.

Reprints and permissions information is available at http://www.nature.com/reprints

Publisher's note Springer Nature remains neutral with regard to jurisdictional claims in published maps and institutional affiliations.

Open Access This article is licensed under a Creative Commons Attribution-NonCommercial-NoDerivatives 4.0 International License, which permits any non-commercial use, sharing, distribution and reproduction in any medium or format, as long as you give appropriate credit to the original author(s) and the source, provide a link to the Creative Commons licence, and indicate if you modified the licensed material. You do not have permission under this licence to share adapted material derived from this article or parts of it. The images or other third party material in this article are included in the article's Creative Commons licence, unless indicated otherwise in a credit line to the material. If material is not included in the article's Creative Commons licence and your intended use is not permitted by statutory regulation or exceeds the permitted use, you will need to obtain permission directly from the copyright holder. To view a copy of this licence, visit http://creativecommons.org/licenses/by-nc-nd/4.0/.

© The Author(s) 2026

This Article in Press is shared early to give you faster access to new research. It is citable and carries a permanent DOI. The final edited version will replace it automatically.

Control of out-of-plane anti-damping spin torque with a canted ferromagnetic spin source

Xiaoxi Huang[1,†,*], Daniel A. Pharis[1,†], Hang Zhou[2], Zishen Tian[3,8], Thow Min Jerald Cham[1], Zhaoyang Wang[4], Yuhan Liang[1], Kyoungjun Lee[5], Yilin Evan Li[6], Maciej Olszewski[1], Di Yi[4], Chang-Beom Eom[5], Darrell G. Schlom[6,7,10], Lane W. Martin[3,8,9], Ding-Fu Shao[2], and Daniel C. Ralph[1,7,*]

[1]Department of Physics, Cornell University, Ithaca, NY 14853, USA
[2]Key Laboratory of Materials Physics, Institute of Solid-State Physics, HFIPS, Chinese Academy of Sciences, Hefei 230031, China
[3]Department of Materials Science and Engineering, University of California, Berkeley, CA 94720, USA
[4]State Key Laboratory of New Ceramics and Fine Processing, School of Materials Science and Engineering, Tsinghua University, Beijing 100084, China
[5]Department of Materials Science and Engineering, University of Wisconsin-Madison, Wisconsin 53706, USA
[6]Department of Materials Science and Engineering, Cornell University, Ithaca, NY 14853, USA
[7]Kavli Institute at Cornell for Nanoscale Science, Ithaca, NY 14853, USA
[8]Rice Advanced Materials Institute, Rice University, Houston, TX 77005, USA
[9]Department of Materials Science and NanoEngineering, Chemistry, and Physics and Astonomy, Rice University, Houston, TX 77005, USA
[10]Leibniz-Institut für Kristallzüchtung, Max-Born-Str. 2, 12489 Berlin, Germany.
[†]These authors contributed equally: Xiaoxi Huang, Daniel A. Pharis
[*]Corresponding authors: xh384@cornell.edu, dcr14@cornell.edu

Contents

1 Magnetic domain structure of $SrRuO_3$ thin films **2**

2 Determining magnetic easy axis from angle dependent magnetoresistance **6**

3 Exchange coupling between $SrRuO_3$ and Py **8**

4 Details of the ST-FMR analysis **9**

5 Suppression of ξ_{DL}^{z} by domains **13**

6 ST-FMR measurements at room temperature **16**

7 Second-harmonic Hall measurements **17**

8 Current-induced magnetization switching **17**

9 Vector components of the field-like torque **22**

10 Temperature dependent analysis **23**

11 Survey of out-of-plane damping-like torque **26**

12 DFT analysis of spin-orbit torque in $SrRuO_3$ **26**

1 Magnetic domain structure of $SrRuO_3$ thin films

$SrRuO_3$ has an orthorhombic structure with a=5.5670Å, b=5.5304Å, c=7.8446Å, $\alpha = 90°$, $\beta = 90°$, and $\gamma = 89.6°$. When $SrRuO_3$ is grown on a (001)-oriented $SrTiO_3$ substrate, it can grow on the substrate with its $(001)_o$, $(110)_o$, or $(1\bar{1}0)$ planes (o denotes orthorhomic index) parallel to the (001) plane of the substrate, thus leading to six possible orthorhombic domains (A, A′, B, B′, C, C′)[1]. Fig. S1a shows an example of the A type domain, demonstrating the epitaxial relationship. For the A domain, the epitaxial relationship is $SrRuO_3$ $[110]_o$ ∥ $SrTiO_3$ [001], $SrRuO_3$ $[\bar{1}10]_o$ ∥ $SrTiO_3$ [100], and $SrRuO_3$ $[001]_o$ ∥ $SrTiO_3$ [010]. The epitaxial relationships of the six structural domains are summarized in Fig. S1b.

To investigate the domain structure of a 22 nm thick $SrRuO_3$ (SRO) films grown on (001)-oriented $SrTiO_3$ (STO) substrate, X-ray reciprocal space mapping (RSM) around the 103 family of peaks of the substrate was carried out (Fig. S2). The SRO thin film and STO substrate have the same in-plane lattice parameter from all the diffraction peaks, indicating that the SRO thin film is coherently strained in the plane. The downshift of 103 and upshift of $\bar{1}03$ with respect to the 013 and $0\bar{1}3$ peaks confirm the orthorhombic crystal structure of SRO thin film; and no impurity peaks are observed, suggesting that this 22 nm thick SRO thin film is single-domain (A type) within the detection limit of the lab X-ray[2, 3].

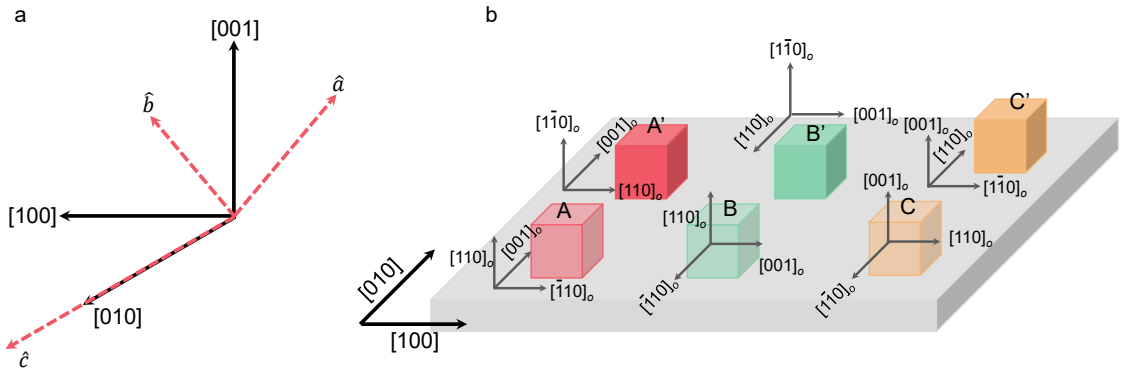


Fig. S1. Schematic demonstration of six possible orthorhombic domains of $SrRuO_3$ grown on a perovskite $SrTiO_3$ substrate. a, Epitaxial relationship of $SrRuO_3$ A domain on $SrTiO_3(001)$ substrate. a, b, and c are the unit vectors of the $SrRuO_3$ orthorhombic unit cell. b, Six possible structural domains on (001)-oriented $SrTiO_3$ substrate.

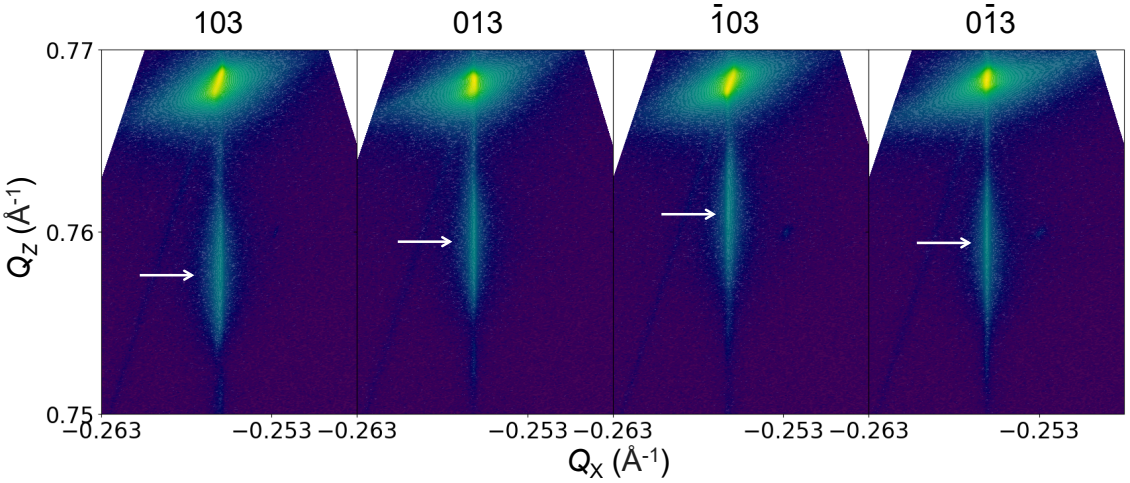


Fig. S2. Structural domain of a $SrTiO_3(001)/SrRuO_3$ (22 nm) sample. Reciprocal space mapping (RSM) of 103, 013, $\bar{1}03$, and $0\bar{1}3$ of the sample. The white arrows indicate the diffraction peaks from A domain.

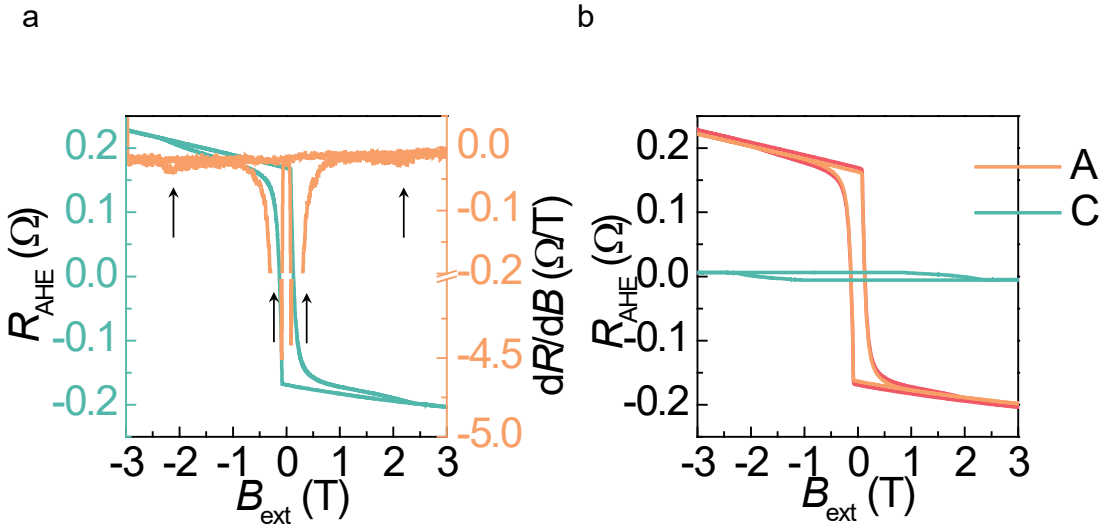


Fig. S3. Anomalous Hall effect in STO(001)/SRO (22 nm) sample at 70 K. a, Anomalous Hall resistance and first derivative of the anomalous Hall resistance as a function of field. The black arrows indicate the coercivities of A and C domains. b, Simulated anomalous Hall resistance as a function of field for A and C domains.

According to Wang et al. [3], magnetic domains in $SrRuO_3$ predominantly stem from structural domains due to the large magneto-crystalline anisotropy of $SrRuO_3$. Because of the distinct orientations of different structural domains, the associated magnetic domains will have different coercive fields. Therefore, characterization the magnetization switching behavior of $SrRuO_3$ thin films will be another effective way to reveal the magnetic domain structure of $SrRuO_3$. The anomalous Hall resistance and its first derivative for the 22 nm thick $SrRuO_3$ sample are shown in Fig. S3a. A multi-step switching behavior is most clearly seen from the first derivative of anomalous Hall resistance, suggesting that two types of domains with different coercivities coexist in the 22 nm thick SRO sample, which seems to contradict the conclusion drawn from the RSM measurements. Nonetheless, an analysis of the population of these two types domains (Fig. S3b) reveals that the minor domain (C domain) makes up less than 5% of the entire sample, beyond the detection limit of the lab X-ray. We will use measurements of the anomalous Hall resistance and its first derivative as one way to quantify the population of magnetic domains with different coercivities.

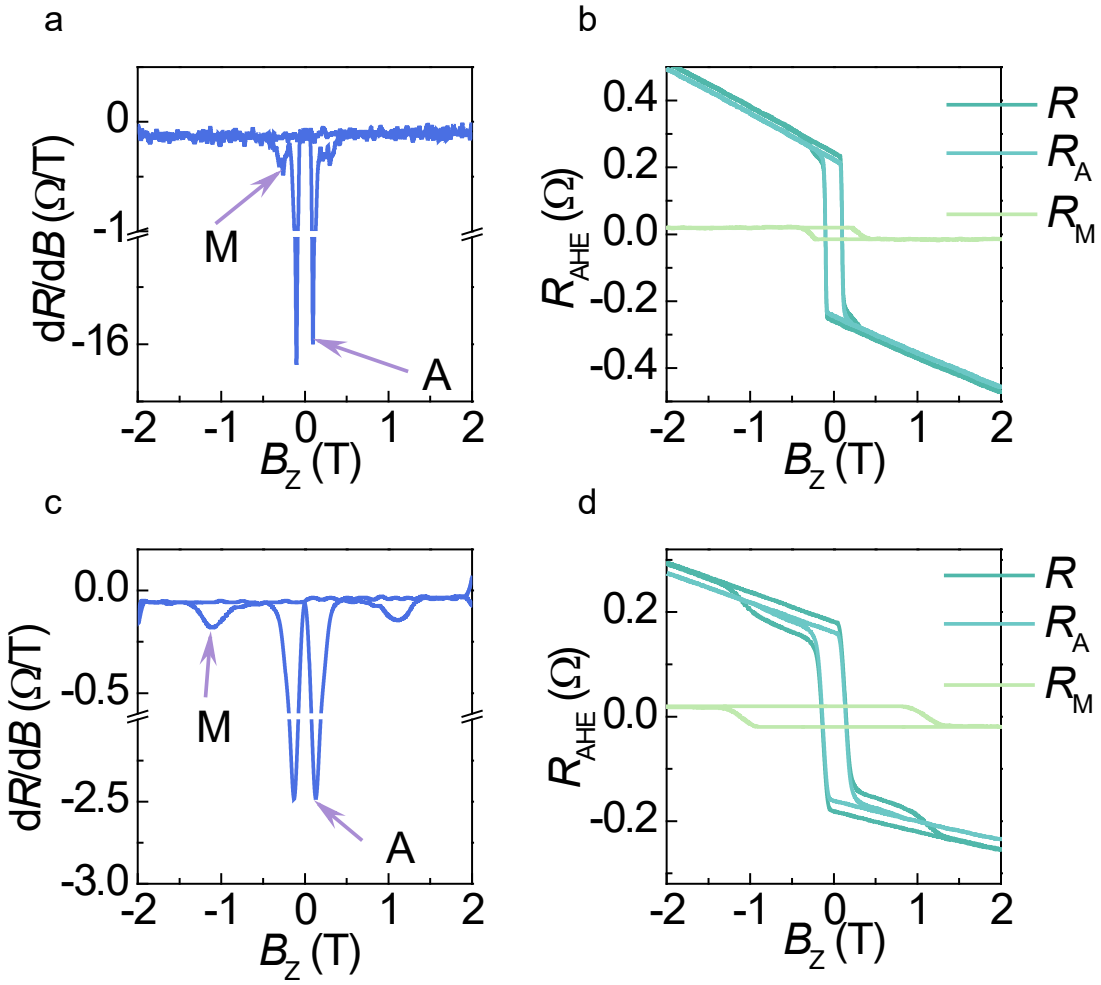


Fig. S4. Domain structure characterized using anomalous Hall effect measurements. a, The first derivative of anomalous Hall resistance as a function of external magnetic field for a single-layer 5 nm $SrRuO_3$ thin film at 110 K. 'A' denotes the dominant domain and 'M' denotes minor domains present in the sample. b, Anomalous Hall resistance for the same single-layer 5 nm $SrRuO_3$ thin film at 110 K. R_A and R_M are the contributions from the 'A' domain and the minor domain to the anomalous Hall resistance. c, The first derivative of anomalous Hall resistance as a function of external magnetic field for a 10 nm $SrRuO_3$ thin film at 110 K. d, Anomalous Hall resistance for the same 10 nm $SrRuO_3$ film at 110 K.

2 Determining magnetic easy axis from angle dependent magnetoresistance

To determine the orientation of the magnetic easy axis of the $SrRuO_3$ thin films, angle dependent magnetoresistance measurements were carried out. The longitudinal voltage (V_{XX}) was measured as the external magnetic field was rotated in a plane (YZ plane) perpendicular to the applied current direction (X) (see Fig. S5a). If the magnetization tilt direction is aligned with the YZ plane in which the applied magnetic field rotates (i.e., $\phi_m = 0°$), then the magnetic moment jumps abruptly at an angle θ_0, resulting in sudden change in resistance. In this $\phi_m = 0°$ case, the center of the hysteretic magnetoresistance indicates the magnetic hard axis [4, 5]. For samples in which the device orientation is different relative to the crystal axes so that the $\phi_m \neq 0°$, the angle at which the resistance jump occurs shifts gradually toward $\theta_0 = 90°$ as ϕ_m approaches 90°. Using this approach, the angle of the projection of the magnetization onto the sample plane can be determined based on where θ_0 has a minimum value, and for this case θ_0 denotes the direction of the hard axis. This is the method by which we identify that our predominantly single-domain samples have the magnetization tilted from the $[001]_{pc}$ direction toward $[100]_{pc}$. Example magnetoresistance measurements for a predominantly single-domain 20 nm sample with $\phi_m = 0°$ (corresponding to $\psi = 90°$) and $\phi_m = 90°$ ($\psi = 0°$) are shown in Fig. S5b. A macrospin simulation of the rotation of the magnetic moment for $\phi_m = 0°$ is shown in Fig. S5c, in good agreement with the experimental result in Fig. S5b for the positions of the magnetization jumps. A summary of the simulated values of θ_0 for 20 nm devices oriented to have different angles ψ relative to the $SrRuO_3$ crystal axes is shown in Fig. S5d. The experimental results show a similar trend to the simulated results.

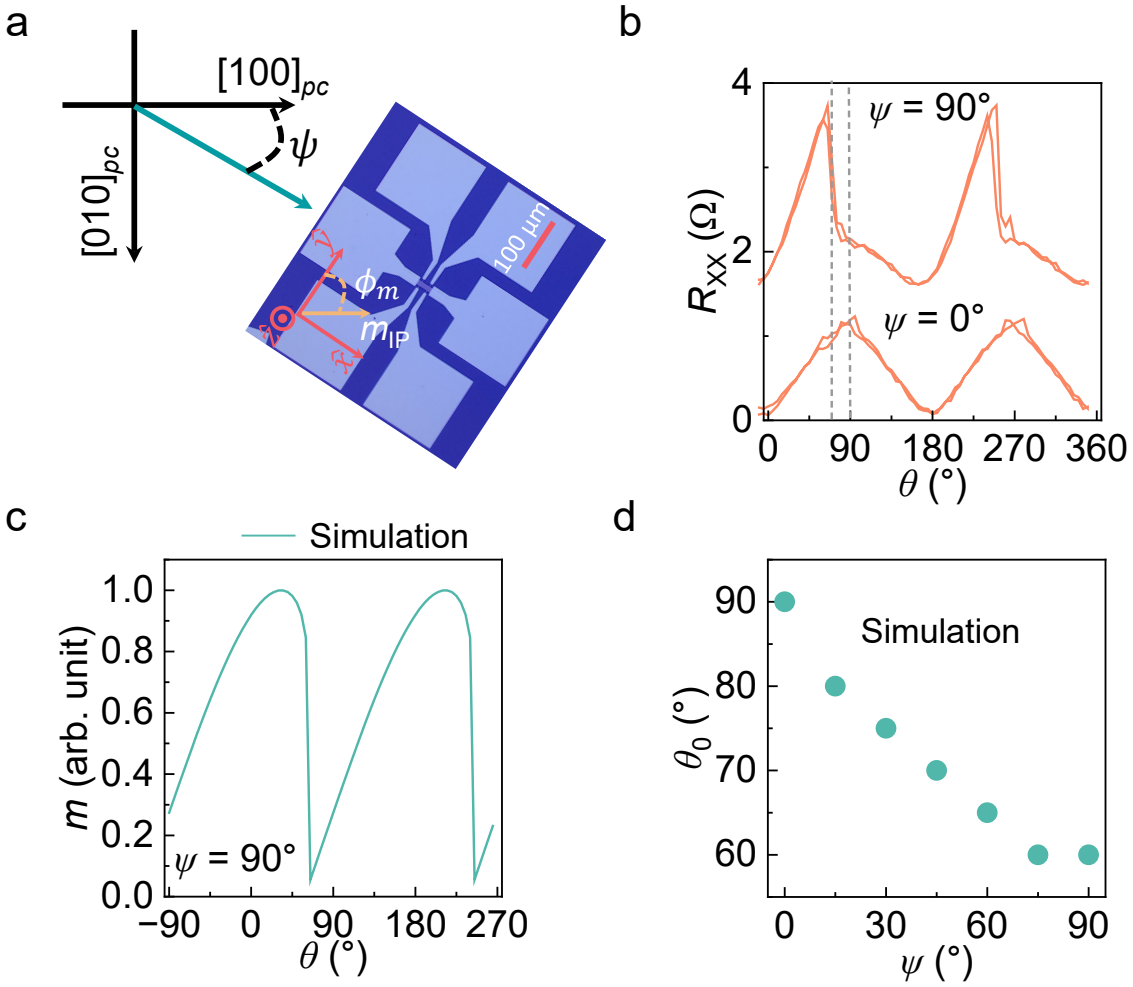


Fig. S5. Magnetic easy axis canting direction and canting angle determination. a, Measurement geometry for determining the tilt angle for the magnetization. m_{IP}: magnetization projection in the plane; ϕ_{m}: angle between m_{IP} and the Y axis of the Hall bar device. b, Example of angle-dependent magnetoresistance measurements for a 20 nm $SrRuO_3$ sample for which $\phi_{\mathrm{m}} = 0°$ (i.e., $\psi = 90°$) and $\phi_{\mathrm{m}} = 90°$ (i.e., $\psi = 0°$). c, A simulation of the magnetoresistance measurement for $\phi_{\mathrm{m}} = 0°$. d, Results of a macrospin calculation for the magnetic-field angles at which the resistance jumps as a function of in-plane device angles, corresponding to the sample in panel b.

3 Exchange coupling between $SrRuO_3$ and Py

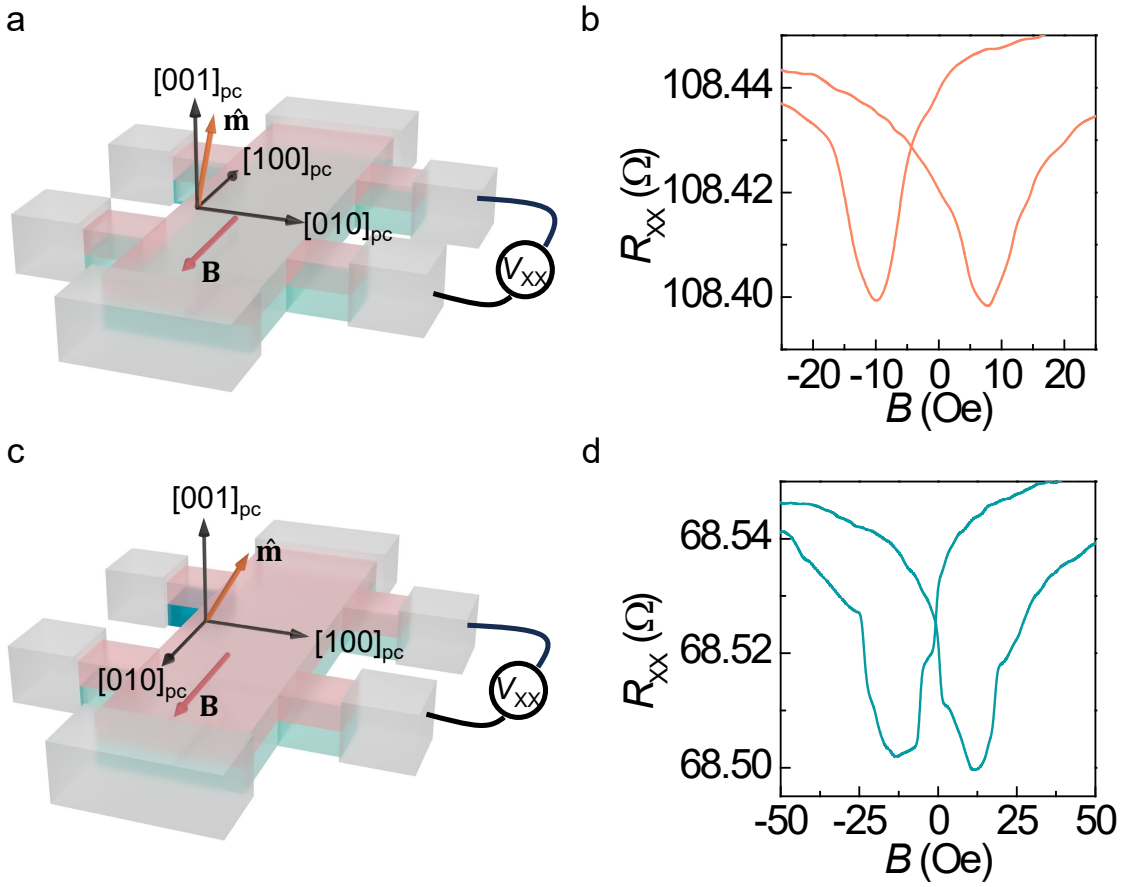


Fig. S6. A check for exchange coupling between $SrRuO_3$ (10 nm) and Py (5 nm). a, Schematic illustration of the measurement geometry to test for exchange coupling along the $[100]_{pc}$ direction. Longitudinal voltage (V_{XX}) is measured while an external magnetic field is swept along the $[100]_{pc}$ direction. b, Measured longitudinal resistance as a function of external magnetic field at 80 K for the geometry in panel a. Two dips are observed, at 8 Oe and −10 Oe, indicating the absence of any significant exchange bias along the $[100]_{pc}$ direction. c, Measurement geometry to test for exchange coupling along the $[010]_{pc}$ direction. d, Measured longitudinal resistance as a function of external magnetic field at 80 K for the geometry in panel c. Two dips are observed symmetrically located at ±13 Oe, indicating the absence of exchange bias along $[010]_{pc}$ direction.

4 Details of the ST-FMR analysis

For the ST-FMR measurements, devices with different in-plane orientations were patterned on the same sample chip and magnetic field angle-dependent ST-FMR measurements were performed on each device. The low temperature ST-FMR measurements were carried out in a home-built cryostat cooled by liquid nitrogen. For each device with a different angle (ψ) of the applied current relative to the $[100]_{\rm pc}$ direction, an ST-FMR scan was performed with the applied magnetic field oriented at an angle φ to the applied microwave current, and such measurements were repeated at values of φ spaced every 10 degrees from 0° to 170°. Then the same angle-dependent ST-FMR measurements were conducted on devices with other values of ψ, ranging from 0° to 165° at every 15 degrees.

The torques acting on the free-layer ferromagnet excite its magnetic moment away from equilibrium, causing a time-dependent resistance of the bilayer due to the anisotropic magnetoresistance in the free-layer ferromagnet. The mixing of the time-dependent resistance with the alternating current produces a d.c. voltage, $V_{\rm mix}$, with the form [6–8]

$$V_{\rm XX}^{\rm mix} = \frac{I_{\rm rf} R_{\rm AMR}}{2\alpha\omega^{+}} \sin 2\varphi \Big[S(B)\tau_{\text{in-plane}}(\varphi) + A(B)\frac{\omega_2}{\omega}\tau_{\text{out-of-plane}}(\varphi) \Big], \tag{1}$$

where $I_{\rm rf}$ is the microwave current amplitude flowing within the device, $R_{\rm XX} = R_0 + R_{\rm AMR}\cos^2\varphi$ is the anisotropic magnetoresistance (AMR), $\tau_{\text{in-plane}}(\varphi)$ and $\tau_{\text{out-of-plane}}(\varphi)$ are the in-plane and out-of-plane components of the electric-field-induced torques, $S(B) = \Delta^2/[\Delta^2 + (B - B_0)^2]$ is the symmetric Lorentzian function, $A(B) = (B - B_0)\Delta/[\Delta^2 + (B - B_0)^2]$ is the anti-symmetric Lorentzian function, $\gamma = 2\mu_{\rm B}/\hbar$ is the gyromagnetic ratio, $\Delta = \alpha\omega/\gamma$ is the half-width-at-half-maximum linewidth, $\omega_1 = \gamma B_0$, $\omega_2 = \gamma(B_0 + \mu_0 M_{\rm eff})$, $\omega^{+} = \omega_1 + \omega_2$, and $\omega = \sqrt{\omega_1\omega_2}$ at resonance.

As long as the spin from the electric-field-induced spin current has a fixed orientation independent of the free layer's magnetization direction, then the angle-dependence of the in-plane and out-of-plane torques can be written in terms of the contributions from the X, Y, and Z spin components as:

$$\tau_{\text{in-plane}}(\varphi) = \tau_{\rm DL,Y}^{0}\cos(\varphi) + \tau_{\rm DL,X}^{0}\sin(\varphi) + \tau_{\rm FL,Z}^{0} \tag{2}$$

$$\tau_{\text{out-of-plane}}(\varphi) = \tau_{\rm FL,Y}^{0}\cos(\varphi) + \tau_{\rm FL,X}^{0}\sin(\varphi) + \tau_{\rm DL,Z}^{0}. \tag{3}$$

The symmetric and anti-symmetric components of $V_{\rm mix}$ contributed by the X, Y, Z components of the torques depend on the magnetic-field angle as:

$$V_{\rm S} = S_{\rm DL}^{\rm X} \sin 2\varphi \sin\varphi + S_{\rm DL}^{\rm Y} \sin 2\varphi \cos\varphi + S_{\rm FL}^{\rm Z} \sin 2\varphi, \tag{4}$$

$$V_{\rm A} = A_{\rm FL}^{\rm X} \sin 2\varphi \sin\varphi + A_{\rm FL}^{\rm Y} \sin 2\varphi \cos\varphi + A_{\rm DL}^{\rm Z} \sin 2\varphi, \tag{5}$$

where $S_{\rm DL}^{\rm X}$, $S_{\rm DL}^{\rm Y}$, $A_{\rm DL}^{\rm Z}$, $A_{\rm FL}^{\rm X}$, $A_{\rm FL}^{\rm Y}$, $S_{\rm FL}^{\rm Z}$ are amplitudes of mixing voltages contributed by X, Y, Z components of damping-like and field-like torques, which can be written as:

$$S_{\rm DL}^{\rm X} = \frac{I_{\rm rf} R_{\rm AMR}}{2\alpha\omega^{+}} \tau_{\rm DL,X}^{0}, \tag{6}$$

$$S_{\rm DL}^{\rm Y} = \frac{I_{\rm rf} R_{\rm AMR}}{2\alpha\omega^{+}} \tau_{\rm DL,Y}^{0}, \tag{7}$$

$$S_{\rm FL}^{\rm Z} = \frac{I_{\rm rf} R_{\rm AMR}}{2\alpha\omega^{+}} \gamma B_{\rm FL,Z}^{0}. \tag{8}$$

$$A_{\rm FL}^{\rm X} = \frac{I_{\rm rf} R_{\rm AMR}}{2\alpha\omega^{+}} \frac{\omega_2}{\omega} \gamma B_{\rm FL,X}^{0}, \tag{9}$$

$$A_{\rm FL}^{\rm Y} = \frac{I_{\rm rf} R_{\rm AMR}}{2\alpha\omega^{+}} \frac{\omega_2}{\omega} \gamma B_{\rm FL,Y}^{0}, \tag{10}$$

$$A_{\rm DL}^{\rm Z} = \frac{I_{\rm rf} R_{\rm AMR}}{2\alpha\omega^{+}} \frac{\omega_2}{\omega} \tau_{\rm DL,Z}^{0}. \tag{11}$$

The vector components of the damping-like torque efficiency can be defined as $\xi_{\rm DL}^{\rm i} = \tau_{\rm DL,i}^{0} \frac{eM_{\rm S} t_{\rm FM}}{\mu_{\rm B} J_{\rm e}}$, where $M_{\rm S}$ (A/m) is the saturation magnetization of the free layer, $t_{\rm FM}$ is the thickness of the free layer, and $J_{\rm e}$ is the charge current density in the spin-source layer. Putting everything together, the damping-like torque efficiencies corresponding to the conventional spin component in the Y direction and the unconventional component in the Z direction can be written:

$$\xi_{\rm DL}^{\rm Y} = S_{\rm DL}^{\rm Y} \frac{eM_{\rm S} t_{\rm FM}}{\hbar J_{\rm e}} \frac{4\Delta}{I_{\rm rf} R_{\rm AMR}} \frac{2B_0 + \mu_0 M_{\rm eff}}{\sqrt{B_0 (B_0 + \mu_0 M_{\rm eff})}} \tag{12}$$

$$\xi_{\rm DL}^{\rm Z} = A_{\rm DL}^{\rm Z} \frac{eM_{\rm S} t_{\rm FM}}{\hbar J_{\rm e}} \frac{4\Delta}{I_{\rm rf} R_{\rm AMR}} \frac{2B_0 + \mu_0 M_{\rm eff}}{B_0 + \mu_0 M_{\rm eff}}, \tag{13}$$

where $S_{\rm DL}^{\rm Y}$ is the Y component of the symmetric mixing voltage ($\propto \sin(2\varphi)\cos(\varphi)$) and $A_{\rm DL}^{\rm Z}$ is the Z component of the anti-symmetric mixing voltage ($\propto \sin(2\varphi)$).

An example ST-FMR measurement at 95 K for a $SrRuO_3$ (30 nm)/Py (5 nm) sample is shown in Fig. S7. The anti-symmetric and symmetric components of the mixing voltage as a function of magnetic field angle are shown in Fig. S7a and b. Both fits require an additional $\sin 2\varphi$ component. The effective magnetization of 0.798 T is returned by a fit to the Kittel equation $f = \frac{\gamma}{2\pi}\sqrt{B_{\text{ext}}(B_{\text{ext}} + \mu_0 M_{\text{eff}})}$(Fig. S7c). To determine the spin-orbit torque efficiencies, it is necessary to determine the microwave current within the sample and the amplitude of the AMR. An example microwave current calibration on the same $SrRuO_3$ (30 nm)/Py (5 nm) is shown in Fig. S7d and e. The longitudinal device resistance was first measured as a function of applied d.c. current from -10 mA to 10 mA (Fig. S7d). Due to Joule heating at large currents, the device resistance increases parabolically with the applied d.c. current. The solid dark blue curve represents a parabolic fit of the data to $R_{\text{XX}} = 0.028 I_{\text{dc}}^2 + 69.069$. To calibrate the strength of microwave current at a given power, the longitudinal device resistance was then measured as a function of the power of the applied microwave current (Fig. S7e). At the ST-FMR measurement power 20 dBm, $R_{\text{XX}} = 70.270\,\Omega$ was measured, which corresponds to a current of root-mean-square (rms) amplitude of $6.506 \times 10^{-3}\ A$. Therefore, at 20 dBm the amplitude of the microwave current within the device is $I_{\text{RF}} = 9.200 \times 10^{-3}\ A$. To calibrate the AMR, the longitudinal device resistance was measured at various in-plane angles of a 1000 Oe magnetic field, as shown in Fig. S7f. The solid curve is a fit to $R_{\text{XX}} = R_{\text{AMR}} \cos^2\varphi + R_0$ with a linear background, yielding $R_{\text{AMR}} = 0.060\,\Omega$. The resistivities of $SrRuO_3$ (30 nm) and Py (5 nm) at 95 K are 117.302 $\mu\Omega$·cm and 69.855 $\mu\Omega$·cm respectively (Fig. S8a). Based on a two parallel resistor model, the current density in the $SrRuO_3$ spin source layer is $J_{\text{e}} = 2.396 \times 10^{10}$ A/m^2. By evaluating Eq. 13 with the measured parameters, Z component of the spin-orbit torque $\sim -0.007 \pm 0.0007$ is returned. Repeating the calibration measurements at a series of temperatures returns the temperature dependent Z component of the damping-like torque (Fig. S8c).

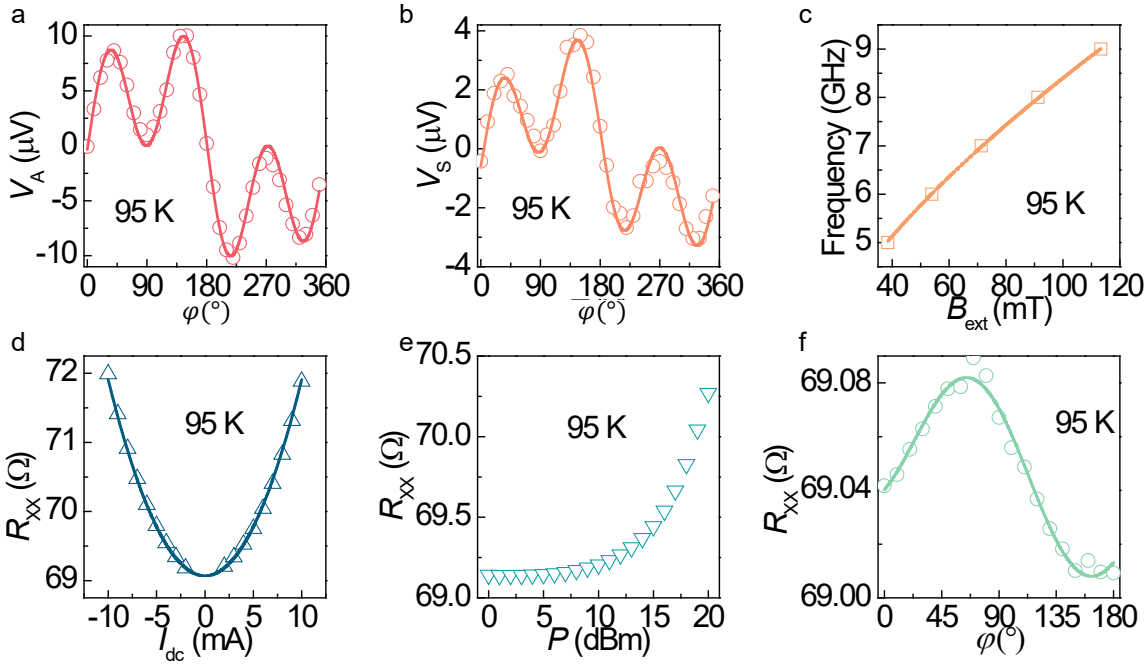


Fig. S7. An example microwave current calibration at 95 K for the sample $SrRuO_3$ (30 nm)/Py (5 nm). a, b, Symmetric and antisymmetric components of the mixing voltage as a function of magnetic field angle (φ). A microwave current of 20 dBm is applied. c, A summary of resonant magnetic field at various microwave frequencies. d, Longitudinal two-point resistance as a function of applied d.c. current. e, Longitudinal two-point resistance as a function of applied microwave power. f, Longitudinal resistance as a function of angle between current and the external magnetic field (1000 Oe).

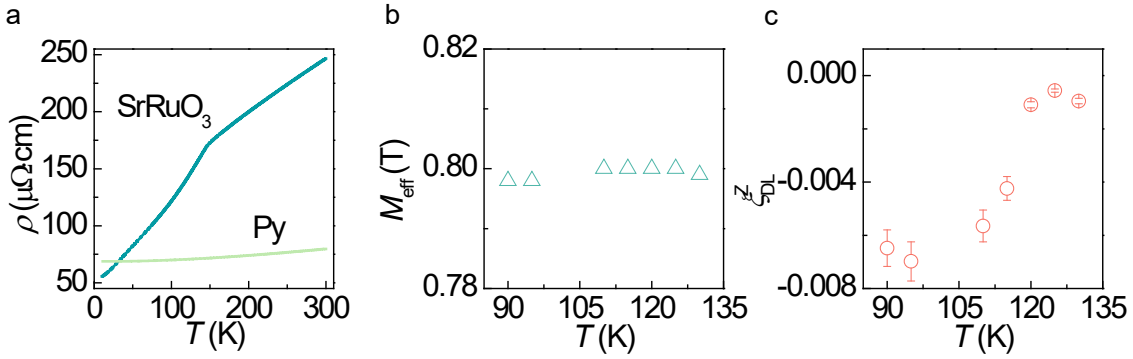


Fig. S8. Temperature dependent spin-orbit torque efficiency calibration for the $SrRuO_3$ (30 nm)/Py (5 nm) sample. a, Temperature dependent resistivities for $SrRuO_3$ (30 nm) and Py (5 nm). b, Temperature dependent effective magnetization for the $SrRuO_3$ (30 nm)/Py (5 nm) sample. c, Temperature dependent out-of-plane damping-like torque efficiency estimated with microwave current calibration. The error bars are from the uncertainties of film thicknesses.

5 Suppression of ξ_{DL}^{Z} by domains

This section discusses the results for two 10 nm $SrRuO_3$ samples for which the $SrRuO_3$ depositions resulted in non-single-domain films. For the sample shown in Fig. S9, the characterization of the magnetization tilt angle using an applied magnetic field rotating in the $[001]_{pc}$-$[100]_{pc}$ plane looks similar to the single-domain samples with a jump in resistance near $\theta_0 = 130°$, but the resistance jump does not shift to $\theta_0 = 90°$ for a magnetic-field rotation in the perpendicular $[001]_{pc}$-$[010]_{pc}$ plane as expected for a single-domain sample with the magnetization tilted within the $[001]_{pc}$-$[100]_{pc}$ plane. (See the discussion of Fig. S5b in Supplementary Section 2.) Instead, the magnetoresistance sweep for the $[001]_{pc}$-$[010]_{pc}$ plane also has a jump near $\theta_0 = 130°$. This suggests that the sample contains a mixture of B-type domains as well as A-type (see Fig. S1). For this sample the out-of-plane damping-like torque is suppressed; see representative antisymmetric ST-FMR amplitudes in Figs. S9c and d.

Another example of ξ_{DL}^{Z} suppressed by the presence of domains is demonstrated in Fig. S10. The anomalous Hall sweep for this $SrRuO_3$ (10 nm)/Py (5 nm) sample consists of several steplike changes, indicating a mix of domain types with distinct coercive fields (Fig. S10a). The resulting out-of-plane damping-like torque efficiency is also essentially zero for this mixed-domain sample. (Fig. S10b)

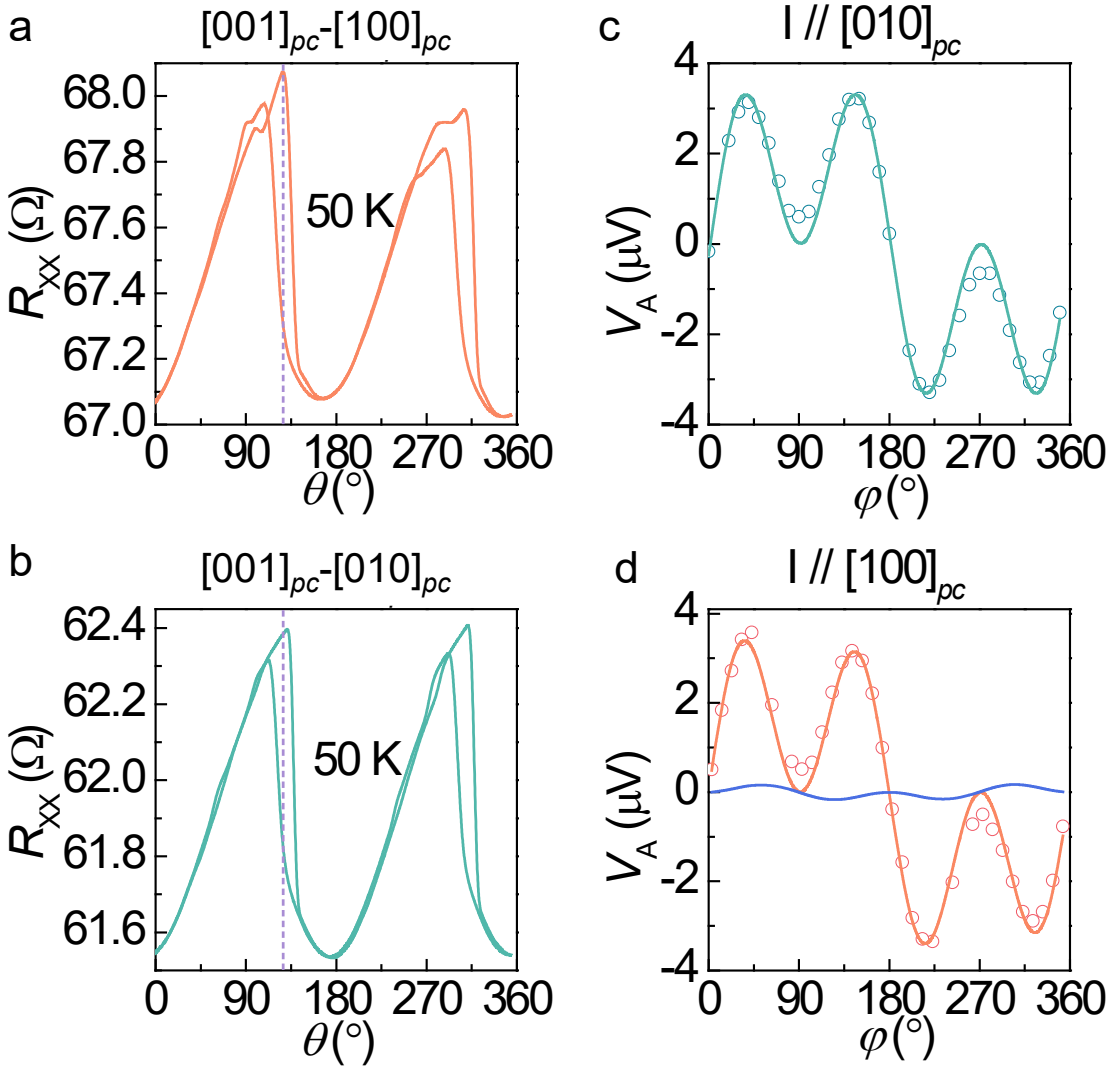


Fig. S9. Suppression of ξ_{DL}^{Z} by the presence of domains in a 10 nm $SrRuO_3$ film. a, Magnetoresistance measurement at 50 K for a $SrRuO_3$ (10 nm)/Py (5 nm) sample. A d.c. current of 100 μA is applied along $[010]_{pc}$ direction. The external magnetic field is rotating within the $[001]_{pc}$-$[100]_{pc}$ plane. The magnetic easy axis appears to be canted 40° away from $[001]_{pc}$ toward the $[010]_{pc}$ direction. b, The same magnetoresistance measurement on a device from the same wafer with d.c. current applied along the $[100]_{pc}$ direction. The magnetic easy axis here appears to cant 40° away from $[001]_{pc}$ toward the $[010]_{pc}$ direction, instead of having the switching angle shift to 90°. The combined results of panels a and b therefore suggest a mix of A and B-type domains. c, Anti-symmetric component of the mixing voltage at various magnetic field angle for the device with current oriented along the $[010]_{pc}$ direction. The data are fitted to $\sin 2\varphi \cos\varphi$ and the fit is improved by adding a small $\sin 2\varphi \sin\varphi$ component (X component of the field-like torque) but no Z component of damping-like torque. d, Anti-symmetric component of the mixing voltage at various magnetic field angle for the device with current oriented along the $[100]_{pc}$ direction. The data are fitted to $\sin 2\varphi \cos\varphi$ and the quality of the fit is not improved by adding more terms.

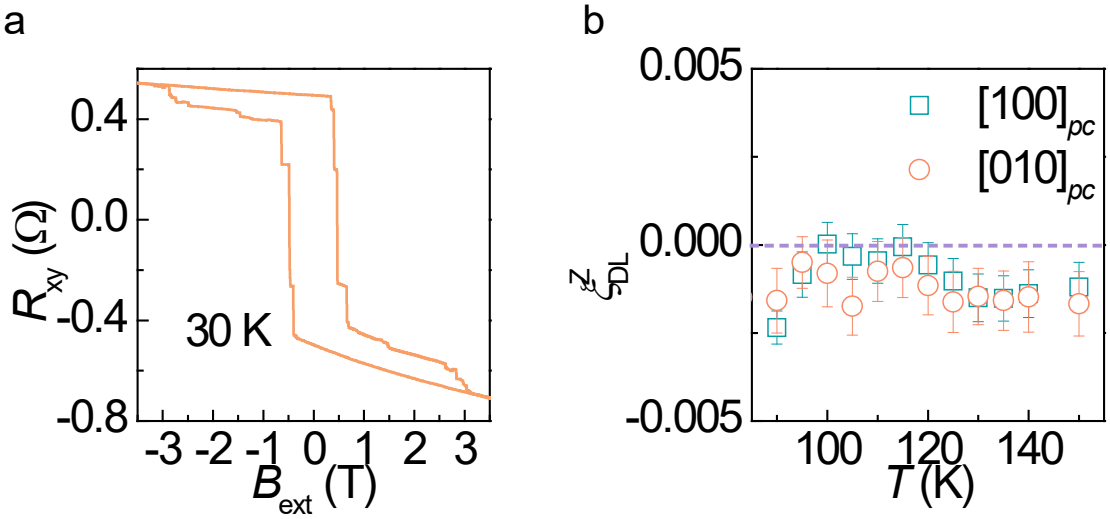


Fig. S10. Suppression of ξ^{Z}_{DL} by the presence of domains in a second 10 nm $SrRuO_3$ film. a, An example anomalous Hall resistance as a function of external magnetic field swept in the out-of-plane direction at 30 K. A multi-step switching pattern is observed, indicating the presence of multiple domains with comparable populations having different coercive fields. b, The out-of-plane damping-like torque efficiencies (ξ^{Z}_{DL}) as a function of temperature for the device oriented along both $[100]_{pc}$ and $[010]_{pc}$ directions are negligible in this sample. The error bars are from the uncertainties of film thicknesses.

6 ST-FMR measurements at room temperature

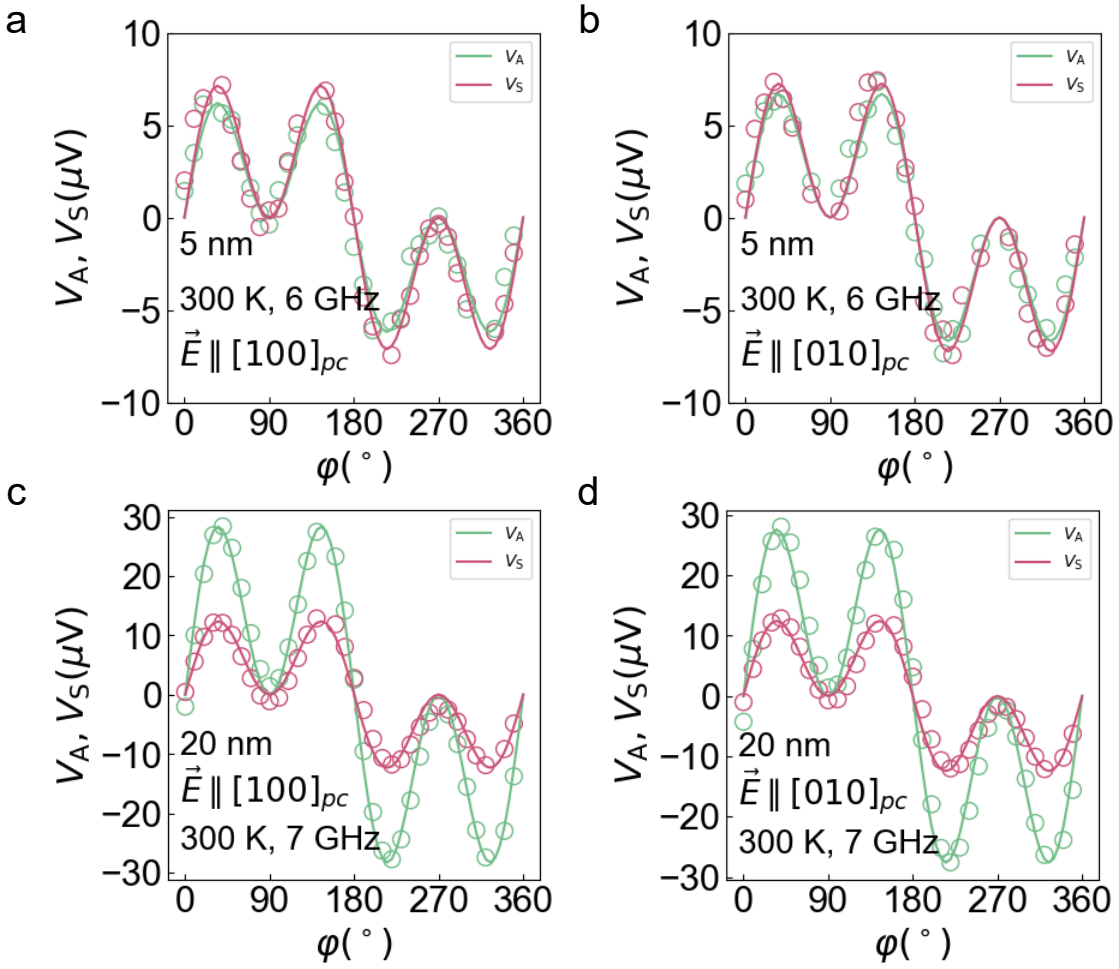


Fig. S11. ST-FMR measurements at room temperature for samples $SrRuO_3$ (5, 20 nm)/Py (5 nm). a, b, Anti-symmetric and symmetric components of the mixing voltage for electric fields applied along $[100]_{pc}$ and $[010]_{pc}$ for $SrRuO_3$ (5 nm)/Py (5 nm). The solid curve is a fit to the Y component, proportional to $\sin(2\varphi)\cos(\varphi)$. c, d, Anti-symmetric and symmetric components of the mixing voltage for electric fields applied along $[100]_{pc}$ and $[010]_{pc}$ for $SrRuO_3$ (20 nm)/Py (5 nm). The solid curve is a fit to the Y component, proportional to $\sin(2\varphi)\cos(\varphi)$

7 Second-harmonic Hall measurements

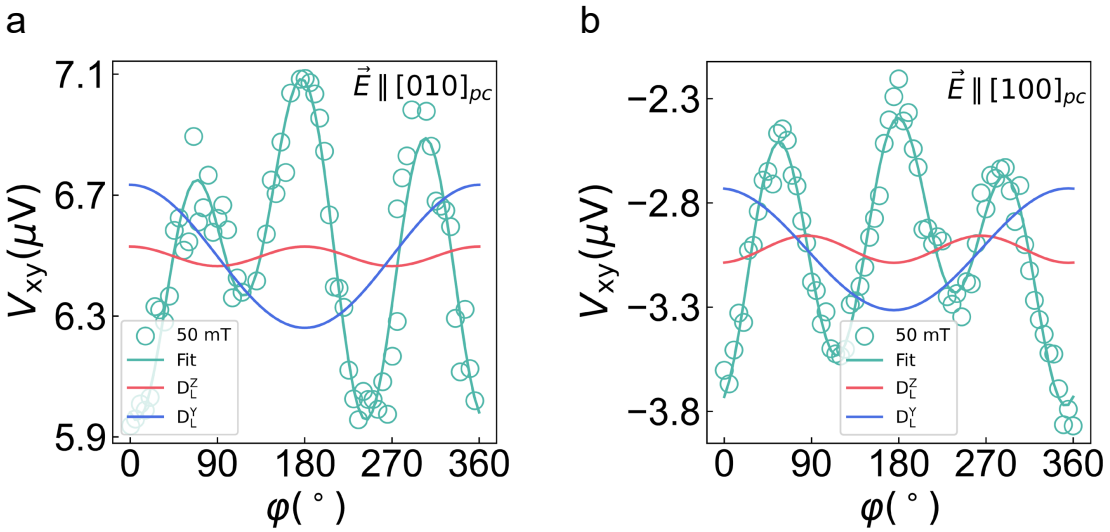


Fig. S12. Second harmonic Hall voltage measurements for the sample $SrRuO_3$ (5 nm)/Py (5 nm) at 100 K. a, b, Second harmonic Hall voltages (V_{xy}) as a function of the in-plane orientation (φ) of a magnetic field of 50 mT for electric field ($\vec{\mathbf{E}}$) along $[010]_{pc}$ and $[100]_{pc}$ respectively.

8 Current-induced magnetization switching

When using the conventional in-plane component of spin-orbit torque to drive switching of a perpendicularly-magnetized magnet in a micron-scale device via domain wall motion, an out-of-plane anti-damping torque component can provide the symmetry breaking needed to make the switching deterministic. To confirm the presence of out-of-plane anti-damping torque from $SrRuO_3$, we performed current-induced magnetization switching measurements for a magnet with perpendicular magnetic anisotropy (PMA) consisting of Ti/$Co_{20}Fe_{60}B_{20}$/MgO (2 nm)/Pd (1.5 nm). A stable PMA was achieved over a range of thicknesses for the Ti (2, 3, 4, 5 nm) and $Co_{20}Fe_{60}B_{20}$ (1.1 nm, 1.2 nm, 1.3 nm). The Pd served as a capping layer.

A control sample consisting of Pt (5 nm)/Ti (3 nm)/$Co_{20}Fe_{60}B_{20}$ (1.1 nm)/MgO (2 nm)/Pd (1.5 nm) was first made. The as-grown sample had a magnetic coercivity

approximately 6 Oe, which was enhanced to 160 Oe (Fig. S13a) after a baking at 180 °C for 5 minutes during device fabrication. The Hall resistance was recorded after sending current pulses of 1 ms into a Hall-bar device with a 10-μm-wide current channel and 2-μm-wide Hall leads. Since Pt produces only conventional anti-damping torque confined within the sample plane, in order to deterministically switch the magnetization of the PMA magnet a small external magnetic field needs to be applied along the current direction to provide the necessary symmetry breaking. As shown in Fig. S13b and c, the magnetization of the PMA magnet was reversibly switched by current pulses with an assisting magnetic field of 100 Oe applied along the current direction, and the switching polarity was flipped by reversing the direction of the applied magnetic field. No deterministic magnetization switching was observed when no symmetry-breaking magnetic field was applied (Fig. S13d).

We confirmed that symmetry breaking from out-of-plane anti-damping torque from $SrRuO_3$ can enable field-free magnetization switching of a PMA magnet for a sample with the layer structure $SrRuO_3$ (10 nm)/Ti (5 nm)/$Co_{20}Fe_{60}B_{20}$ (1.2 nm)/MgO (2 nm)/Pd (1.5 nm) as illustrated in Fig. S14a. 5 nm of Ti was used to inhibit coupling between the two magnets as shown in Fig. S15a. The Hall-bar device used in magnetization switching measurement is shown in Fig. S14b: the width of the current channel is 10 μm and the width of the Hall leads is 2 μm. Magnetization switching driven by a swept out-of-plane magnetic field at 90 K is shown by the anomalous Hall curve in Fig. S14c, with two transitions: one from $SrRuO_3$ and one from $Co_{20}Fe_{60}B_{20}$. That only one step of magnetization switching is observed for $SrRuO_3$ indicates the presence of a single-domain state for this 10 nm $SrRuO_3$ film. Deterministic current-driven switching of the PMA magnet was observed at zero applied external magnetic field at 90 K (Fig. S15b). The switching polarity remained the same (Fig. S15c and d) with external magnetic fields of 30 Oe and -30 Oe applied along the current direction, indicating that the the symmetry breaking from the out-of-plane anti-damping torque was dominant in determining the switching polarity.

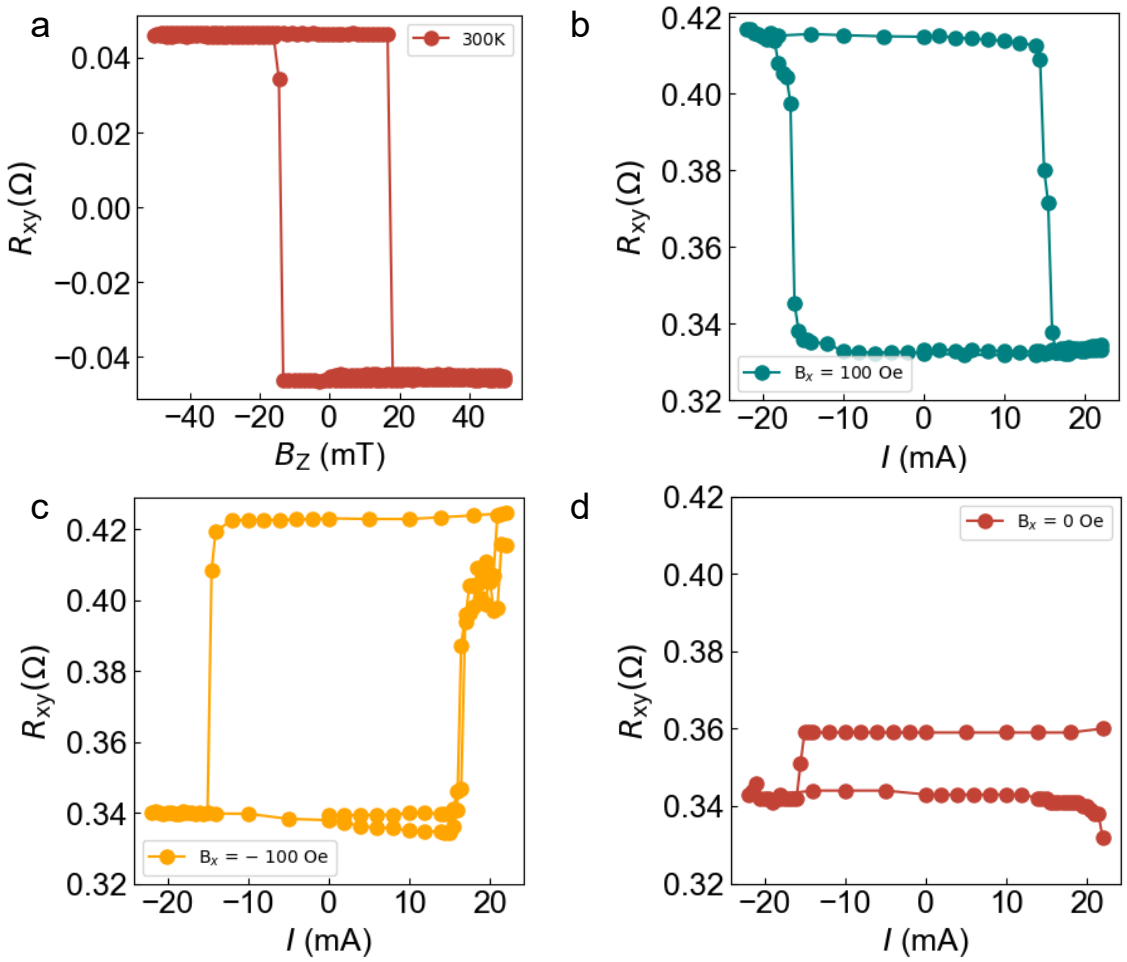


Fig. S13. Magnetization switching of a 10 μm × 30 μm sample of Pt (5 nm)/Ti (3 nm)/$Co_{20}Fe_{60}B_{20}$ (1.1 nm)/MgO (2 nm)/Pd (1.5 nm) at 300 K. a, Hall resistance (R_{xy}) minor loop for switching of the $Co_{20}Fe_{60}B_{20}$ layer as a function of out-of-plane magnetic field. A background resistance is subtracted to make R_{xy} symmetric along the y axis. b, Hall resistance as a function of applied current pulses with a 100 Oe external magnetic field applied along the current direction, demonstrating deterministic switching. The applied current pulses have a duration of 1 ms. c, Hall resistance as a function of applied current pulses with a reversed magnetic field (−100 Oe) along the current direction, for which the direction of switching is reversed. d, Hall resistance as a function of applied current pulses with zero external magnetic field applied, for which deterministic switching is no longer present.

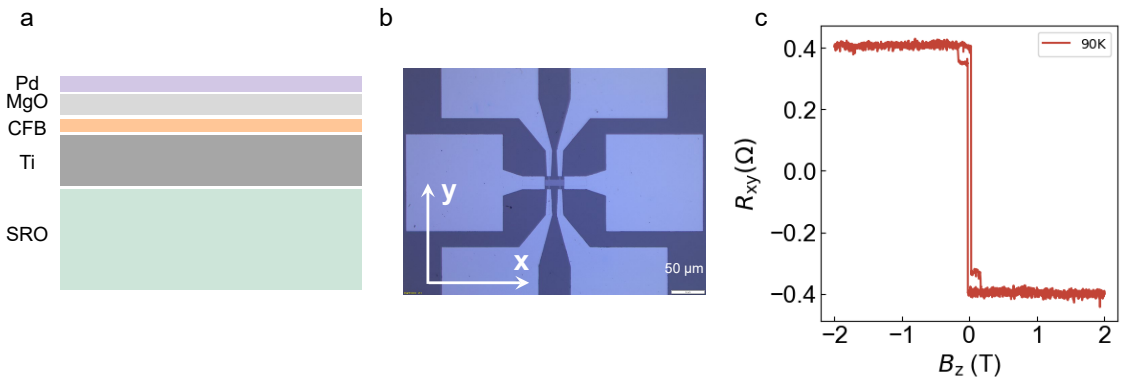


Fig. S14. Field-free magnetization switching: materials stack, device lay-out, and characterization of domain structure. a, Layers in the materials stack, consisting of $SrRuO_3$ (10 nm)/Ti (5 nm)/$Co_{20}Fe_{60}B_{20}$ (1.2 nm)/MgO (2 nm)/Pd (1.5 nm). b, An optical image of the Hall device for magnetization switching experiment. The widths of the current channel and Hall leads are 10 μm and 2 μm respectively. c, Full hysteresis loop for the Hall resistance as a function of external magnetic field swept along the out-of-plane direction at 90 K.

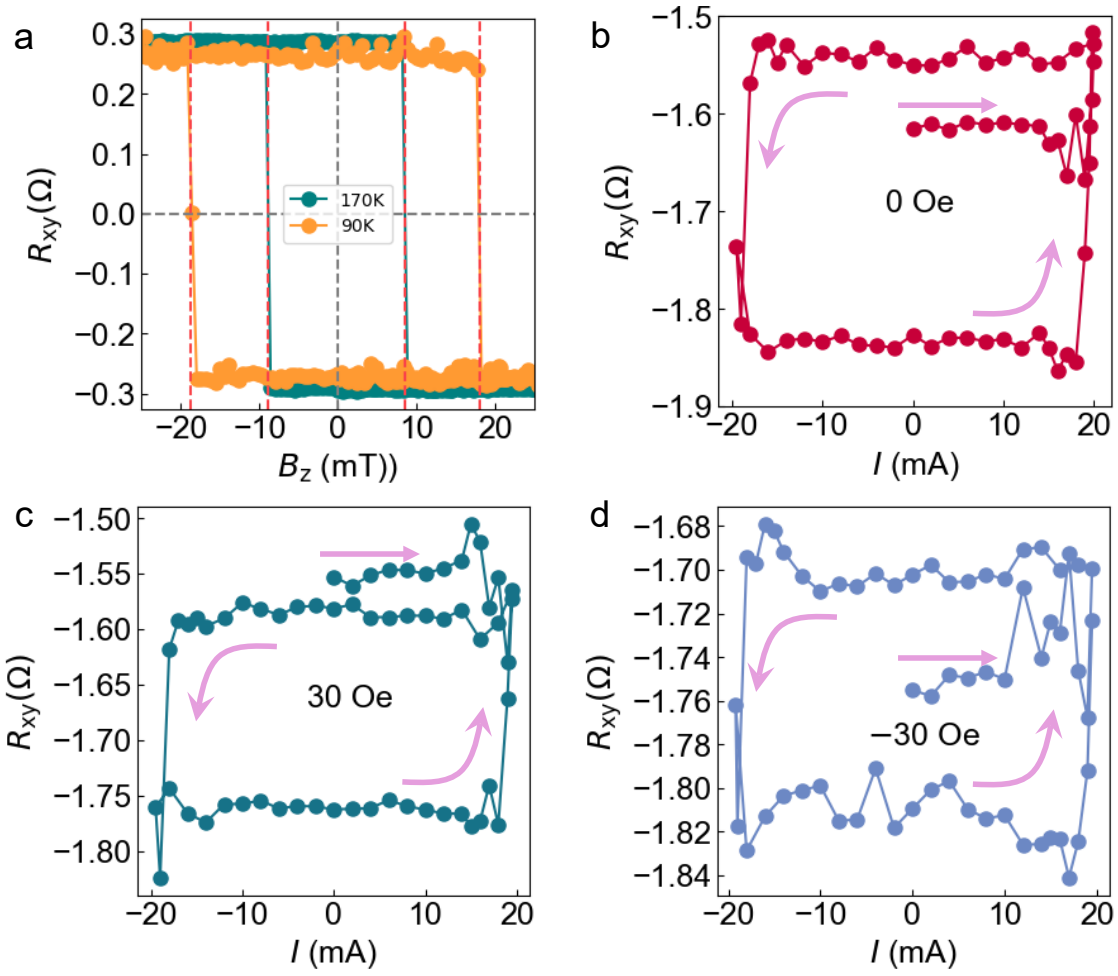


Fig. S15. Field-free magnetization switching of a 10 μm × 30 μm sample of $SrRuO_3$ (10 nm)/Ti (5 nm)/$Co_{20}Fe_{60}B_{20}$ (1.2 nm)/MgO (2 nm)/Pd (1.5 nm). a, Hall resistance (R_{xy}) minor loop for switching the $Co_{20}Fe_{60}B_{20}$ layer as a function of out-of-plane magnetic field at 90 K and 170 K, demonstrating perpendicular magnetic anisotropy. The magnetization reverses at 180 Oe and −187 Oe at 90 K (85 Oe and − 89 Oe at 170 K), indicating the absence of significant exchange coupling between $SrRuO_3$ and $Co_{20}Fe_{60}B_{20}$. A background resistance is subtracted to make R_{xy} symmetric along the y axis. b, Hall resistance as a function of applied current pulses at zero applied external magnetic field and 90 K. The current pulses have a duration of 0.1 ms. c, d, Hall resistance as a function of current pulses at 90 K with external magnetic fields of 30 Oe and -30 Oe applied along the current direction, with the direction of switching unchanged in both cases relative to the 0 Oe case. This indicates that the symmetry-breaking provided by the z-polarized spin current is dominant over the symmetry breaking from a 30 Oe in-plane magnetic field.

9 Vector components of the field-like torque

The efficiencies of the X, Y, and Z components of the field-like torque can be characterized by the amplitude of the respective effective fields per unit applied current density, determined by:

$$\frac{B^0_{\mathrm{FL,\,Z}}}{J_\mathrm{e}} = \frac{S^\mathrm{Z}_\mathrm{FL}}{J_\mathrm{e}} \frac{2\Delta}{I_\mathrm{rf} R_\mathrm{AMR}} \frac{2B_0 + \mu_0 M_\mathrm{eff}}{\sqrt{B_0(B_0 + \mu_0 M_\mathrm{eff})}} \tag{14}$$

$$\frac{B^0_{\mathrm{FL,\,X}}}{J_\mathrm{e}} = \frac{A^\mathrm{X}_\mathrm{FL}}{J_\mathrm{e}} \frac{2\Delta}{I_\mathrm{rf} R_\mathrm{AMR}} \frac{2B_0 + \mu_0 M_\mathrm{eff}}{B_0 + \mu_0 M_\mathrm{eff}} \tag{15}$$

$$\frac{B^0_{\mathrm{FL,\,Y}}}{J_\mathrm{e}} = \frac{A^\mathrm{Y}_\mathrm{FL}}{J_\mathrm{e}} \frac{2\Delta}{I_\mathrm{rf} R_\mathrm{AMR}} \frac{2B_0 + \mu_0 M_\mathrm{eff}}{B_0 + \mu_0 M_\mathrm{eff}} \tag{16}$$

Similarly, the amplitude of the effective field per unit current density for the current-induced Oersted field is given by: $\frac{B_\mathrm{Oe}}{J_\mathrm{e}} = \frac{\mu_0 t_\mathrm{HM}}{2}$.

We find that none of the quantities $\frac{B^0_{\mathrm{FL,X}}}{J_\mathrm{e}}$, $\frac{B^0_{\mathrm{FL,Y}}}{J_\mathrm{e}}$, or $\frac{B^0_{\mathrm{FL,Z}}}{J_\mathrm{e}}$ has any systematic dependence on the angle ψ of the applied electric field relative to the crystal axes. Regarding the unconventional components $\frac{B^0_{\mathrm{FL,X}}}{J_\mathrm{e}}$ and $\frac{B^0_{\mathrm{FL,Z}}}{J_\mathrm{e}}$, they are at our noise level close to zero, and much smaller than the conventional component $\frac{B^0_{\mathrm{FL,Y}}}{J_\mathrm{e}}$. In Fig. S16 we plot the angle-averaged value of $\frac{B^0_{\mathrm{FL,Y}}}{J_\mathrm{e}}$ versus temperature. We see that the conventional field-like component is significantly reduced relative to our estimate of the current-induced Oersted field, which suggests that there is a significant contribution from a field-like spin-orbit torque.

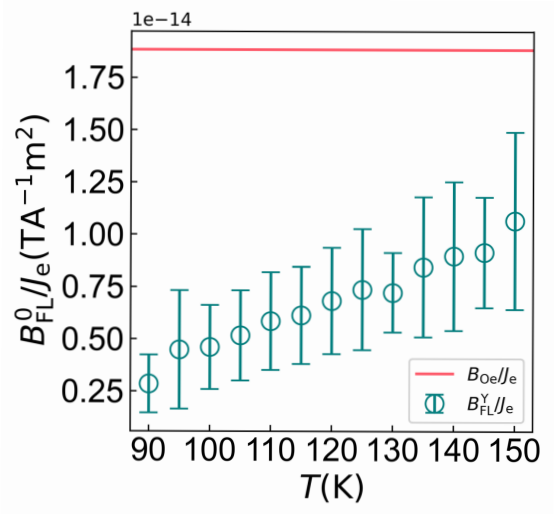


Fig. S16. Conventional (Y-component) field-like torque for the 30 nm thick $SrRuO_3$ sample as a function of temperature. The error bars are from the distribution of $\frac{B^0_{\mathrm{FL,Y}}}{J_e}$ over different angles.

10 Temperature dependent analysis

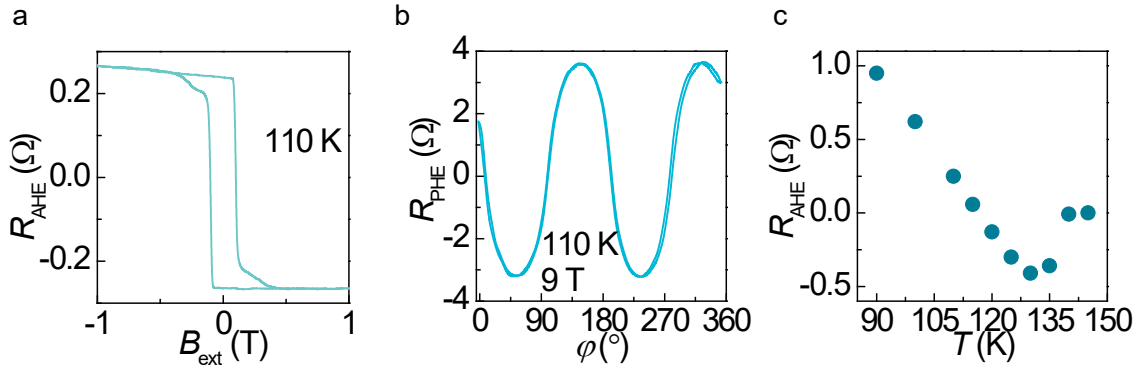


Fig. S17. Anomalous Hall and planar Hall effects. a, Anomalous Hall resistance for a 5 nm $SrRuO_3$ film at 110 K. b, Planar Hall effect for the same 5 nm $SrRuO_3$ sample at 110 K. An external magnetic field of 9 T is applied. c, Anomalous Hall resistance as a function of temperature for the 5 nm $SrRuO_3$ film.

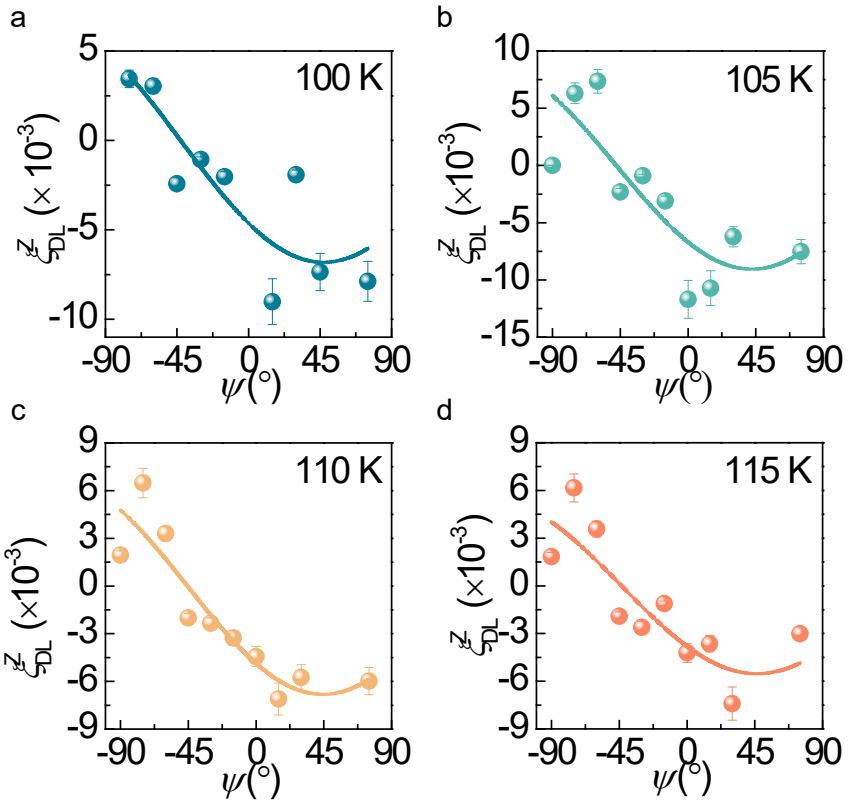


Fig. S18. Measured out-of-plane anti-damping torque efficiencies at various temperatures. a, b, c, d, Out-of-plane damping-like torque efficiency as a function of the angle ψ of the applied electric field at 100 K, 105 K, 110 K and 115 K, respectively. The curves in blue are fits to the data of the form $\xi^z_{DL} = \xi^z_{AHE} \sin\psi + \xi^z_{PHE} \cos\psi$. Error bars are calculated based on the uncertainties of film thicknesses.

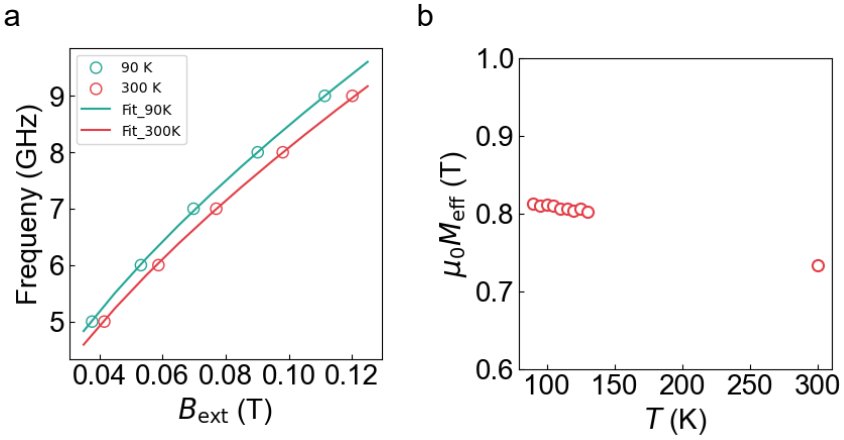


Fig. S19. Effective magnetization analysis for sample $SrRuO_3$ (5 nm)/Py (5 nm). a, Measured resonant magnetic fields as a function of frequency at 300 K and 90 K. The solid curves are Kittel fits (to $f = \gamma/2\pi\sqrt{B_{\text{ext}}(B_{\text{ext}} + \mu_0 M_{\text{eff}})}$). b, Effective magnetization for $SrRuO_3$ (5 nm)/Py (5 nm) as a function of temperature.

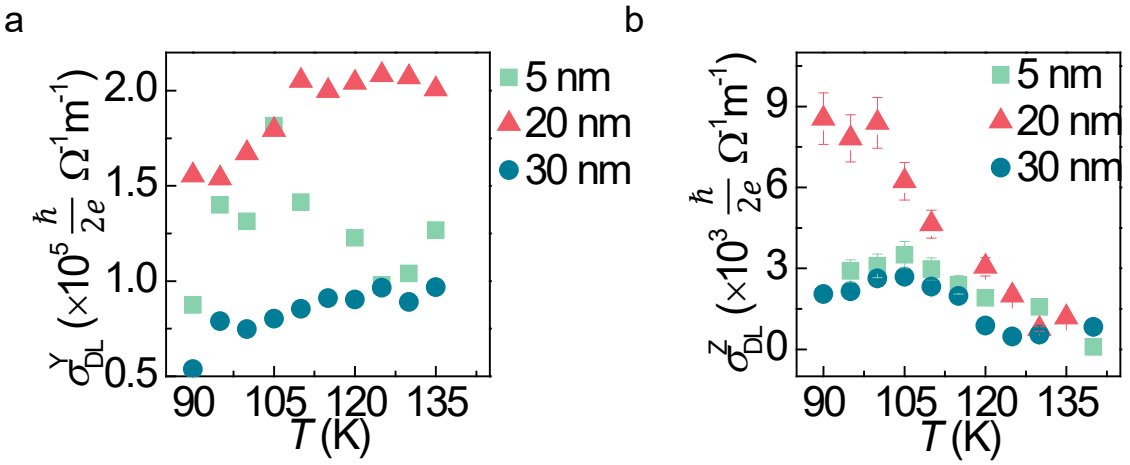


Fig. S20. Spin Hall conductivity for both the Y and Z components of damping-like torque as a function of temperature and film thickness. The error bars are from the uncertainty of film thicknesses.

11 Survey of out-of-plane damping-like torque

Material	ξ^{Z}_{DL}	$\sigma^{Z}_{SH}(\frac{\hbar}{2e})(\Omega m)^{-1}$	$\rho(\mu\Omega cm)$	ref
Low crystal symmetry				
WTe_2	0.014	3.6×10^3	380	[7]
$MoTe_2$	0.008	1.4×10^3	550	[9]
(114) $MnPd_3$	0.008	14×10^3	60	[10]
$PtTe_2/WTe_2$	0.007-0.032	$(17 - 25) \times 10^3$	29-154	[11]
Antiferromagnets				
RuO_2	0.008	6×10^3	140	[8]
Mn_3GaN	0.019	8.6×10^3	220	[12]
Ferromagnets				
$[001]_{pc}$ $SrRuO_3$ (20 nm)	0.013 (100 K)	8.5×10^3	152.7	This work

Table S1: A survey of out-of-plane anti-damping torque in various systems for which quantitative measurements have been reported.

12 DFT analysis of spin-orbit torque in $SrRuO_3$

First we perform a general phenomenological symmetry analysis of the electric-field-driven spin current generation, which can be described as:

$$J^{k}_{j} = \sigma^{k}_{ji} E_i, \tag{17}$$

where where E_i is an electric field along direction i, J^{k}_{j} is the generated spin current flowing along the direction j and polarized along direction k, and σ^{k}_{ji} is the associated spin conductivity. σ^{k}_{ji} can be further decomposed into the time-reversal-even

(T-even) and the time-reversal-odd (T-odd) parts.

There are several mechanisms for the spin current generation. In order to know the T-even/T-odd nature of a mechanism, one can simply check whether the associated $J_{\mathrm{j}}^{\mathrm{k}}$ is invariant under the time reversal symmetry operation, which corresponds to reversing the magnetic moments in the magnetic materials. For example, the $J_{\mathrm{j}}^{\mathrm{k}}$ that originates from Fermi surface (FS) can be described as $J_{j_{\mathrm{FS}}}^{\mathrm{k}} = p_{\mathrm{FS}}^{\mathrm{k}} J_{j_{\mathrm{FS}}}$, where $J_{j_{\mathrm{FS}}}$ is the charge current and $p_{\mathrm{FS}}^{\mathrm{k}}$ is the associated spin polarization. The reversal of magnetic moments flips the spins on FS and changes the sign of $p_{\mathrm{FS}}^{\mathrm{k}}$, so that $J_{j_{\mathrm{FS}}}^{\mathrm{k}}$ is reversed. Therefore, the spin currents driven by the spin-polarized FS in ferromagnets are T-odd. The $J_{\mathrm{j}}^{\mathrm{k}}$ driven by the planar Hall effect (PHE) associated with anisotropic magnetoresistance (AMR) can be described by $J_{j_{\mathrm{PHE}}}^{\mathrm{k}} = p_{\mathrm{PHE}}^{\mathrm{k}} J_{j_{\mathrm{PHE}}}$, where the $J_{j_{\mathrm{PHE}}}$ is the planar Hall current polarized collinear to $\hat{\mathbf{m}}$ and flowing along the direction of $\hat{\mathbf{m}}(\hat{\mathbf{m}} \cdot \mathbf{E})$. Therefore, the reversal of magnetic moments flips $p_{\mathrm{PHE}}^{\mathrm{k}}$ but does not change $J_{j_{\mathrm{PHE}}}$, making $J_{j_{\mathrm{PHE}}}^{\mathrm{k}}$ T-odd.

On the other hand, the $J_{\mathrm{j}}^{\mathrm{k}}$ due to the anomalous Hall effect (AHE) can be described as $J_{j_{\mathrm{AHE}}}^{\mathrm{k}} = p_{\mathrm{AHE}}^{\mathrm{k}} J_{j_{\mathrm{AHE}}}$. Since $J_{j_{\mathrm{AHE}}}$ is along the direction of $\hat{\mathbf{m}} \times \mathbf{E}$ and polarized collinear to $\hat{\mathbf{m}}$, The reversal of magnetic moments flips both $p_{\mathrm{AHE}}^{\mathrm{k}}$ and $J_{j_{\mathrm{AHE}}}$, making $J_{j_{\mathrm{AHE}}}^{\mathrm{k}}$ invariant. Therefore, the spin currents driven by AHE are T-even. Moreover, since the conventional spin Hall effect (SHE) can be roughly understood as the summation of two opposite AHEs, the associated spin current $J_{j_{\mathrm{SHE}}}^{\mathrm{k}}$ is also T-even.

To model the $SrRuO_3$ system numerically, we constructed a orthorhombic $SrRuO_3$ crystal structure, as shown in Fig. S21a. The lattice constants were set to a=5.5670 Å, b =5.5304 Å, and c =7.8446 Å. The magnetic moment was aligned along the b axis.

The electronic-structure calculations were performed within density functional theory (DFT) using the VASP software [13]. The projector-augmented wave (PAW) method was employed [14], and the exchange-correlation energy was treated within the generalized-gradient approximation (GGA) [15] in the Perdew–Burke–Ernzerhof (PBE) form. The plane-wave energy cutoff was set to 600 eV in all calculations. The Brillouin zone was sampled using a 9×9×3 Monkhorst–Pack k-point mesh [16], and the total-energy convergence criterion was set to 10^{-6} eV. Spin-orbit coupling (SOC) was included self-consistently. To account for the electronic correlation effects of Ru 4d orbitals, an effective Hubbard parameter $U_{\mathrm{eff}} = 3.0$ eV as applied to the Ru atoms. The resulting Bloch states were then mapped onto a tight-binding

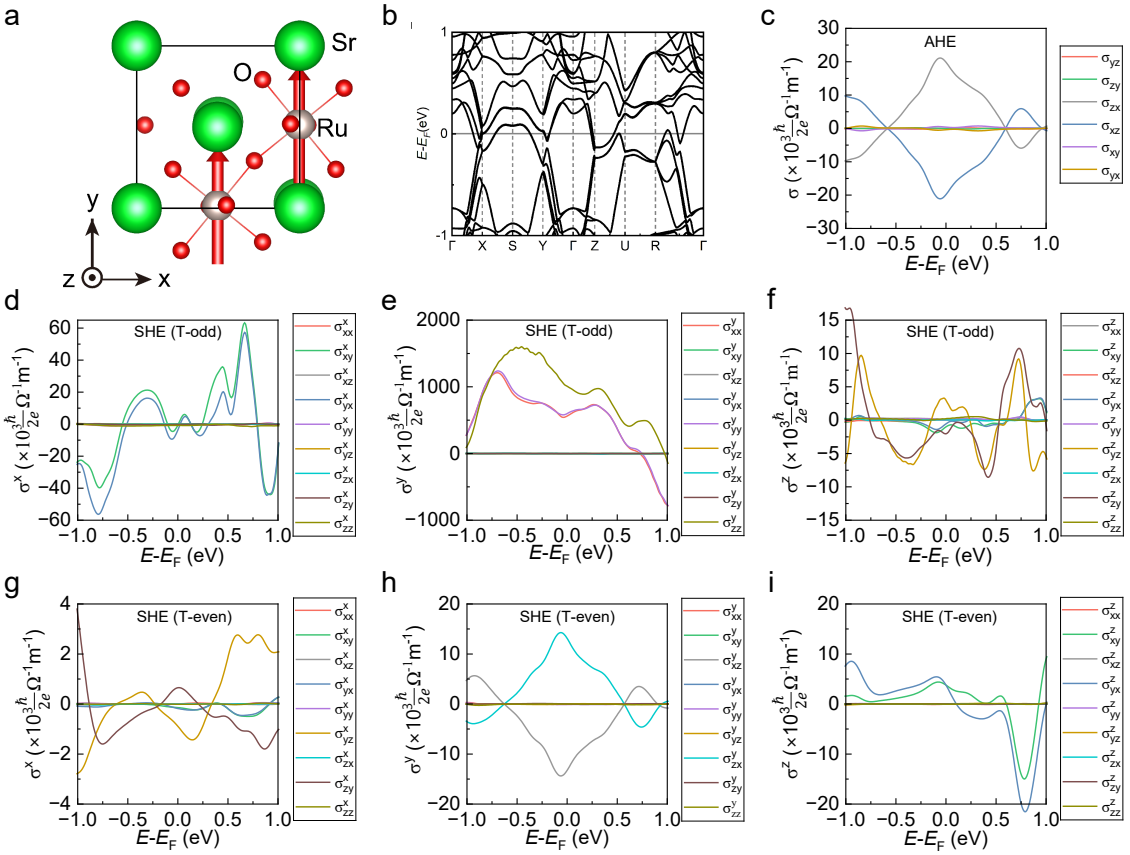


Fig. S21. First principles calculation of spin Hall conductivities due to different mechanisms. a, Orthorhombic unit cell of $SrRuO_3$. x, y, z are defined as $[100]_o$, $[010]_o$ and $[001]_o$ directions. b, Electronic band structure of $SrRuO_3$. c, Spin Hall conductivities contributed by anomalous Hall effect. d, e, f, X, Y, Z components of spin Hall conductivities contributed by T-odd mechanism. g, h, i, X, Y, Z components of spin Hall conductivities contribute by T-even mechanism.

Hamiltonian using the Wannier90 package [17]. The maximally localized Wannier functions were constructed from Ru-d and O-p orbitals. The calculated electronic band structure is shown in Fig. S21b.

The anomalous Hall conductivity (AHC) σ_{ij} where j is the longitudinal electric

field direction and i is the transverse current direction, is calculated as [18]

$$\sigma_{\mathrm{ij}} = \frac{e^2\hbar}{V}\sum_{\mathbf{k}}\sum_{\mathrm{n}\neq\mathrm{m}}\frac{\mathrm{Im}[\langle u_{\mathrm{n}\mathbf{k}}|\hat{\mathbf{v}}_{\mathrm{i}}|u_{\mathrm{m}\mathbf{k}}\rangle\langle u_{\mathrm{m}\mathbf{k}}|\hat{\mathbf{v}}_{\mathrm{j}}|u_{\mathrm{n}\mathbf{k}}\rangle]}{[E_{\mathrm{n}\mathbf{k}}{-}E_{\mathrm{m}\mathbf{k}}]^2}f_{\mathrm{n}\mathbf{k}}, \tag{18}$$

where V is the crystal volume, $\mathbf{k}$ the wave vector, $u_{\mathrm{n}\mathbf{k}}$ the Bloch state, $E_{\mathrm{n}\mathbf{k}}$ the band energy, $f_{\mathrm{n}\mathbf{k}}$ the Fermi-Dirac distribution, and $\hat{\mathbf{v}}_{\mathrm{i}} = \frac{1}{\hbar}\partial H/\partial k_{\mathrm{i}}$ the velocity operator. The time-reversal-odd (T-odd) and time-reversal-even (T-even) spin Hall conductivities (SHC) $\sigma^{\mathrm{k}}_{\mathrm{ij}}$, where j denotes the direction of the applied longitudinal electric field or charge current, i denotes the transverse spin-current flow direction, and k denotes the spin-polarization direction of the spin current, are calculated as [19]

$$\sigma^{\mathrm{k,odd}}_{\mathrm{ij}} = -\frac{e\hbar}{\pi V}\sum_{\mathbf{k}}\sum_{\mathrm{n,m}}\left[\frac{\langle u_{\mathrm{n}\mathbf{k}}|\hat{\mathbf{J}}^{\mathrm{k}}_{\mathrm{i}}|u_{\mathrm{m}\mathbf{k}}\rangle\langle u_{\mathrm{m}\mathbf{k}}|\hat{\mathbf{v}}_{j}|u_{\mathrm{n}\mathbf{k}}\rangle\Gamma^2}{[(E_{\mathrm{F}}-E_{\mathrm{n}\mathbf{k}})^2+\Gamma^2][(E_{\mathrm{F}}-E_{\mathrm{m}\mathbf{k}})^2+\Gamma^2]}\right], \tag{19}$$

$$\sigma^{\mathrm{k,even}}_{\mathrm{ij}} = \frac{2e\hbar}{V}\sum_{\mathbf{k}}\sum_{\mathrm{n}\neq\mathrm{m}}\frac{\mathrm{Im}[\langle u_{\mathrm{n}\mathbf{k}}|\hat{\mathbf{J}}^{\mathrm{k}}_{\mathrm{i}}|u_{\mathrm{m}\mathbf{k}}\rangle\langle u_{\mathrm{m}\mathbf{k}}|\hat{\mathbf{v}}_{\mathrm{j}}|u_{\mathrm{n}\mathbf{k}}\rangle]}{[E_{\mathrm{n}\mathbf{k}}-E_{\mathrm{m}\mathbf{k}}]^2}f_{\mathrm{n}\mathbf{k}}, \tag{20}$$

where $\hat{\mathbf{J}}^{\mathrm{k}}_{\mathrm{i}} = \frac{1}{2}\{\hat{\mathbf{s}}_{\mathrm{k}}, \hat{\mathbf{v}}_{\mathrm{i}}\}$ is the spin current operator with $\hat{\mathbf{s}}_{\mathrm{k}}$ the k-component of the spin operator, E_{F} the Fermi energy and Γ the constant broadening parameter. The PHE-related tensor was not evaluated in the present work, because it is closely related to AMR and therefore requires a microscopic treatment of spin-dependent scattering, which lies beyond the scope of the present calculation framework.

We used the broadening parameter $\Gamma = 0.05$ eV. The AHC and SHC tensors were evaluated on a dense 70×70×50 k-point mesh to ensure convergence. The results for σ_{ij} and $\sigma^{\mathrm{k}}_{\mathrm{ij}}$ relative to the orthorhombic crystal axes are listed in Table S2, where the x, y, and z directions are defined by the $[100]_{\mathrm{o}}$, $[010]_{\mathrm{o}}$, and $[001]_{\mathrm{o}}$ directions. The calculated values as a function of electron energy are shown in Fig. S21c-i.

The calculated AHC and SHC tensors for $SrRuO_3$ films with different growth orientations and charge-current directions were obtained from those of the reference $SrRuO_3$(o) film using a rotation matrix D. For the AHC tensor, the transformation is given by

$$\sigma^{(\mathrm{pc})}_{\mathrm{ij}} = \sum_{\mathrm{l,m}} D_{\mathrm{il}}D_{\mathrm{jm}}\sigma^{(\mathrm{o})}_{\mathrm{lm}}, \tag{21}$$

where (o) denotes the orthorhombic coordinate system and (pc) denotes the pseudocubic coordinate system. For the SHC tensor, the transformation is

$$\sigma^{\mathrm{k,(pc)}}_{\mathrm{ij}} = \sum_{\mathrm{l,m,n}} D_{\mathrm{il}}D_{\mathrm{jm}}D_{\mathrm{kn}}\sigma^{\mathrm{n,(o)}}_{\mathrm{lm}}. \tag{22}$$

Here, $D_{\rm il}$, $D_{\rm jm}$, and $D_{\rm kn}$ transform the transverse spin-current direction, the longitudinal charge-current direction, and the spin-polarization direction, respectively. In this convention, i always represents the transverse charge-current or spin-current flow direction, j represents the longitudinal applied electric-field or charge-current direction, and k represents the spin-polarization direction of the spin current. The AHC and SHC tensors relative to the pseudocubic crystal axes are listed in Table S3, where the x, y, and z directions are defined by the $[100]_{\rm pc}$, $[010]_{\rm pc}$, and $[001]_{\rm pc}$ directions.

In a SOT device, only the spin conductivities $\sigma_{\rm zx}^{\rm x,y,z}$ correspond to vertically-flowing spin currents that produce measurable spin-transfer torques. If we further set the x direction to the in-plane charge current direction away from $[100]_{\rm pc}$ direction by an angle ψ, we derive the ψ-dependent $\sigma_{\rm zx}^{\rm x,y,z}$ of $SrRuO_3$ as shown in Table S4. For the $\sigma_{\rm zx}^{\rm z}$ we focused on in this work, we find $\sigma_{\rm zx}^{\rm z} \sim \cos\psi$ for all T-odd mechanisms and $\sigma_{\rm zx}^{\rm z} \sim \sin\psi$ for all T-even mechanisms.

We note that although the mechanisms discussed above are analyzed separately, they may share the same or similar physical origins. For example, the T-even terms $J_{j_{\rm SHE}}^{\rm k}$ and $J_{j_{\rm AHE}}^{\rm k}$ both stem from Berry curvatures—specifically, the conventional and spin-resolved Berry curvatures, respectively. Similarly, the T-odd terms $J_{j_{\rm FS}}^{\rm k}$ and $J_{j_{\rm PHE}}^{\rm k}$ arise from spin-dependent scattering of conducting electrons on Fermi surfaces. Given these connections, the main text focuses primarily on the unconventional spin currents generated by the AHE and PHE. This simplification offers a practical advantage: it allows us to determine the unconventional spin currents in a ferromagnetic film solely from its magnetization direction, without requiring detailed consideration of crystal or magnetic symmetry groups. The good fit for the angular dependence of the measured $\xi_{\rm DL}^{\rm Z}$ to the form $\xi_{\rm DL}^{\rm Z} = \xi_{\rm PHE}^{\rm Z}\cos\psi + \xi_{\rm AHE}^{\rm Z}\sin\psi$ demonstrates the validity of this analysis.

On the other hand, the conventional $\xi_{\rm DL}^{\rm Y}$ measured in experiments may include various contributions. Besides the conventional SHE in bulk spin source layer, the SHE in the top FM layer and interfacial scattering might also contribute to $\xi_{\rm DL}^{\rm Y}$. Therefore, the measured $\xi_{\rm DL}^{\rm Y}$ may be different to that derived solely from the bulk spin source layer as shown in the Tables.

Table S2: The anomalous Hall conductivity and the spin conductivity tensors of $SrRuO_3$ decomposed into different mechanisms. Here the x, y, and z directions are $[100]_o$, $[010]_o$, and $[001]_o$ directions of the orthorhombic unit cell of $SrRuO_3$, respectively. The spin Hall conductivities listed in the table are given in units of $10^3 \frac{\hbar}{2e} \Omega^{-1}\mathrm{m}^{-1}$ and the anomalous Hall conductivity is listed in units of $10^3\ \Omega^{-1}\mathrm{m}^{-1}$.

	$\sigma_x = \begin{bmatrix} \sigma^x_{xx} & \sigma^x_{xy} & \sigma^x_{xz} \\ \sigma^x_{yx} & \sigma^x_{yy} & \sigma^x_{yz} \\ \sigma^x_{zx} & \sigma^x_{zy} & \sigma^x_{zz} \end{bmatrix}$	$\sigma_y = \begin{bmatrix} \sigma^y_{xx} & \sigma^y_{xy} & \sigma^y_{xz} \\ \sigma^y_{yx} & \sigma^y_{yy} & \sigma^y_{yz} \\ \sigma^y_{zx} & \sigma^y_{zy} & \sigma^y_{zz} \end{bmatrix}$	$\sigma_z = \begin{bmatrix} \sigma^z_{xx} & \sigma^z_{xy} & \sigma^z_{xz} \\ \sigma^z_{yx} & \sigma^z_{yy} & \sigma^z_{yz} \\ \sigma^z_{zx} & \sigma^z_{zy} & \sigma^z_{zz} \end{bmatrix}$
T-odd(SHE)	$\begin{bmatrix} 0 & -1.23 & 0 \\ -4.43 & 0 & 0 \\ 0 & 0 & 0 \end{bmatrix}$	$\begin{bmatrix} 557.79 & 0 & 0 \\ 0 & 594.49 & 0 \\ 0 & 0 & 1013.34 \end{bmatrix}$	$\begin{bmatrix} 0 & 0 & 0 \\ 0 & 0 & 3.12 \\ 0 & -2.05 & 0 \end{bmatrix}$
AHE	$\begin{bmatrix} 0 & 0 & 0 \\ 0 & 0 & 0 \\ 0 & 0 & 0 \end{bmatrix}$	$\begin{bmatrix} 0 & 0 & -20.05 \\ 0 & 0 & 0 \\ 20.05 & 0 & 0 \end{bmatrix}$	$\begin{bmatrix} 0 & 0 & 0 \\ 0 & 0 & 0 \\ 0 & 0 & 0 \end{bmatrix}$
T-even(SHE)	$\begin{bmatrix} 0 & 0 & 0 \\ 0 & 0 & -0.87 \\ 0 & 0.65 & 0 \end{bmatrix}$	$\begin{bmatrix} 0 & 0 & -13.42 \\ 0 & 0 & 0 \\ 13.29 & 0 & 0 \end{bmatrix}$	$\begin{bmatrix} 0 & 3.85 & 0 \\ 3.95 & 0 & 0 \\ 0 & 0 & 0 \end{bmatrix}$

Table S3: The anomalous Hall conductivity and the spin conductivity tensors of $SrRuO_3$ decomposed into different mechanisms. Here the x, y, and z directions are $[100]_{\rm pc}$, $[010]_{\rm pc}$, and $[001]_{\rm pc}$ directions of the pseudo-cubic unit cell of $SrRuO_3$, respectively. The spin Hall conductivities listed in the table are given in units of $10^3 \frac{\hbar}{2e} \Omega^{-1}\mathrm{m}^{-1}$ and the anomalous Hall conductivity is listed in units of $10^3\ \Omega^{-1}\mathrm{m}^{-1}$.

	$\sigma_{\rm x} = \begin{bmatrix} \sigma^{\rm x}_{\rm xx} & \sigma^{\rm x}_{\rm xy} & \sigma^{\rm x}_{\rm xz} \\ \sigma^{\rm x}_{\rm yx} & \sigma^{\rm x}_{\rm yy} & \sigma^{\rm x}_{\rm yz} \\ \sigma^{\rm x}_{\rm zx} & \sigma^{\rm x}_{\rm zy} & \sigma^{\rm x}_{\rm zz} \end{bmatrix}$	$\sigma_{\rm y} = \begin{bmatrix} \sigma^{\rm y}_{\rm xx} & \sigma^{\rm y}_{\rm xy} & \sigma^{\rm y}_{\rm xz} \\ \sigma^{\rm y}_{\rm yx} & \sigma^{\rm y}_{\rm yy} & \sigma^{\rm y}_{\rm yz} \\ \sigma^{\rm y}_{\rm zx} & \sigma^{\rm y}_{\rm zy} & \sigma^{\rm y}_{\rm zz} \end{bmatrix}$	$\sigma_{\rm z} = \begin{bmatrix} \sigma^{\rm z}_{\rm xx} & \sigma^{\rm z}_{\rm xy} & \sigma^{\rm z}_{\rm xz} \\ \sigma^{\rm z}_{\rm yx} & \sigma^{\rm z}_{\rm yy} & \sigma^{\rm z}_{\rm yz} \\ \sigma^{\rm z}_{\rm zx} & \sigma^{\rm z}_{\rm zy} & \sigma^{\rm z}_{\rm zz} \end{bmatrix}$
T-odd (SHE)	$\begin{bmatrix} 403.93 & 0 & 14.05 \\ 0 & 714.15 & 0 \\ 11.78 & 0 & 408.13 \end{bmatrix}$	$\begin{bmatrix} 0 & 2.20 & 0 \\ -1.44 & 0 & -1.45 \\ 0 & 2.21 & 0 \end{bmatrix}$	$\begin{bmatrix} 410.66 & 0 & 11.90 \\ 0 & 718.93 & 0 \\ 14.16 & 0 & 406.84 \end{bmatrix}$
AHE	$\begin{bmatrix} 0 & 10.02 & 0 \\ -10.02 & 0 & 9.96 \\ 0 & -9.96 & 0 \end{bmatrix}$	$\begin{bmatrix} 0 & 0 & 0 \\ 0 & 0 & 0 \\ 0 & 0 & 0 \end{bmatrix}$	$\begin{bmatrix} 0 & 10.09 & 0 \\ -10.09 & 0 & 10.02 \\ 0 & -10.02 & 0 \end{bmatrix}$
T-even (SHE)	$\begin{bmatrix} 0 & 7.14 & 0 \\ -6.97 & 0 & 6.27 \\ 0 & -6.23 & 0 \end{bmatrix}$	$\begin{bmatrix} -3.90 & 0 & 0.02 \\ 0 & 0 & 0 \\ -0.07 & 0 & 3.90 \end{bmatrix}$	$\begin{bmatrix} 0 & 6.33 & 0 \\ -6.37 & 0 & 6.97 \\ 0 & -7.14 & 0 \end{bmatrix}$

Table S4: The ψ-dependent spin conductivities $\sigma^{\rm x}_{\rm zx}$, $\sigma^{\rm y}_{\rm zx}$, and $\sigma^{\rm z}_{\rm zx}$ of $SrRuO_3$ with different mechanisms.

		$\sigma^{\rm x}_{\rm zx}$	$\sigma^{\rm y}_{\rm zx}$	$\sigma^{\rm z}_{\rm zx}$
T-odd	SHE	$D\cos^2\psi + I\sin^2\psi$	$(-D+I)\cos\psi\sin\psi$	$M\cos\psi$
	PHE	$P\cos^2\psi$	$-P\cos\psi\sin\psi$	$Q\cos\psi$
T-even	AHE	$-T\cos\psi\sin\psi$	$-T\sin^2\psi$	$-S\sin\psi$
	SHE	$(Y+BB)\sin\psi\cos\psi$	$BB\cos^2\psi - Y\sin^2\psi$	$-V\sin\psi$

References

1. Jiang, J., Tian, W., Pan, X., Gan, Q. & Eom, C. Domain structure of epitaxial $SrRuO_3$ thin films on miscut (001) $SrTiO_3$ substrates. *Appl. Phys. Lett.* **72,** 2963–2965 (1998).
2. Vailionis, A., Siemons, W. & Koster, G. Strain-induced single-domain growth of epitaxial $SrRuO_3$ layers on $SrTiO_3$: A high-temperature x-ray diffraction study. *Appl. Phys. Lett.* **91,** 071907 (2007).
3. Wang, W. *et al.* Magnetic domain engineering in $SrRuO_3$ thin films. *npj Quantum Mater.* **5,** 73 (2020).
4. Lu, W., Yang, P., Song, W. D., Chow, G. M. & Chen, J. S. Control of oxygen octahedral rotations and physical properties in $SrRuO_3$ films. *Phys. Rev. B* **88,** 214115 (2013).
5. Liu, L. *et al.* Current-induced magnetization switching in all-oxide heterostructures. *Nat. Nanotechnol.* **14,** 939–944 (2019).
6. Karimeddiny, S., Mittelstaedt, J. A., Buhrman, R. A. & Ralph, D. C. Transverse and longitudinal spin-torque ferromagnetic resonance for improved measurement of spin-orbit torque. *Phys. Rev. Appl.* **14,** 024024 (2020).
7. MacNeill, D. *et al.* Control of spin-orbit torques through crystal symmetry in WTe_2/ferromagnet bilayers. *Nat. Phys.* **13,** 300–305 (2017).
8. Bose, A. *et al.* Tilted spin current generated by the collinear antiferromagnet ruthenium dioxide. *Nat. Electron.* **5,** 267–274 (2022).
9. Stiehl, G. M. *et al.* Layer-dependent spin-orbit torques generated by the centrosymmetric transition metal dichalcogenide β-$MoTe_2$. *Phys. Rev. B* **100,** 184402 (2019).
10. DC, M. *et al.* Observation of anti-damping spin-orbit torques generated by in-plane and out-of-plane spin polarizations in $MnPd_3$. *Nat. Mater.* **22,** 591–598 (2023).
11. Wang, F. *et al.* Field-free switching of perpendicular magnetization by two-dimensional $PtTe_2/WTe_2$ van der Waals heterostructures with high spin Hall conductivity. *Nat. Mater.* **23,** 768–774 (2024).
12. Nan, T. *et al.* Controlling spin current polarization through non-collinear antiferromagnetism. *Nat. Commun.* **11,** 4671 (2020).
13. Kresse, G. & Furthmüller, J. Efficient iterative schemes for ab initio total-energy calculations using a plane-wave basis set. *Phys. Rev. B* **54,** 11169 (1996).

14. Kresse, G. & Joubert, D. From ultrasoft pseudopotentials to the projector augmented-wave method. *Phys. Rev. B* **59,** 1758 (1999).

15. Perdew, J. P., Burke, K. & Ernzerhof, M. Generalized gradient approximation made simple. *Phys. Rev. Lett.* **77,** 3865 (1996).

16. Monkhorst, H. J. & Pack, J. D. Special points for Brillouin-zone integrations. *Phys. Rev. B* **13,** 5188 (1976).

17. Mostofi, A. A. *et al.* An updated version of wannier90: A tool for obtaining maximally-localised Wannier functions. *Comput. Phys. Commun.* **185,** 2309–2310 (2014).

18. Yao, Y. *et al.* First principles calculation of anomalous Hall conductivity in ferromagnetic bcc Fe. *Phys. Rev. Lett.* **92,** 037204 (2004).

19. Freimuth, F., Blügel, S. & Mokrousov, Y. Spin-orbit torques in Co/Pt(111) and Mn/W(001) magnetic bilayers from first principles. *Phys. Rev. B* **90,** 174423 (2014).